Spring 2015

Control oriented concentrating solar power (CSP) plant model and its applications

Qi Luo
Purdue University

Graduate School Form 30
(Revised 08/14)

PURDUE UNIVERSITY
GRADUATE SCHOOL
Thesis/Dissertation Acceptance

This is to certify that the thesis/dissertation prepared

By Qi Luo

Entitled
CONTROL ORIENTED CONCENTRATING SOLAR POWER (CSP) PLANT MODEL AND ITS APPLICATIONS

For the degree of Doctor of Philosophy

Is approved by the final examining committee:

Kartik Ariyur

Suresh Garimella

Sugato Chakravarty

Athula Kulatunga

To the best of my knowledge and as understood by the student in the Thesis/Dissertation Agreement, Publication Delay, and Certification/Disclaimer (Graduate School Form 32), this thesis/dissertation adheres to the provisions of Purdue University's "Policy on Integrity in Research" and the use of copyrighted material.

Kartik Ariyur

Approved by Major Professor(s): _____

_____

Approved by: Anil Bajaj 02/17/2015

Head of the Department Graduate Program Date

CONTROL ORIENTED CONCENTRATING SOLAR POWER (CSP) PLANT MODEL AND ITS APPLICATIONS

A Dissertation

Submitted to the Faculty

of

Purdue University

by

Qi Luo

In Partial Fulfillment of the

Requirements for the Degree

of

Doctor of Philosophy

May 2015

Purdue University

West Lafayette, Indiana

I dedicate my dissertation work to my family. A special gratitude to my loving parents, Piduo Luo and Guangxia Niu who have inspired me to be a man of integrity, a man of mercy and responsibility, and a man keeps in pursuit of knowledge.

I also dedicate this dissertation and give special thanks to my advisor professor Kartik Ariyur. Without his broad knowledge, his patient tutoring, especially without his daring adventure spirit, I could not have finished this thesis.

ACKNOWLEDGMENTS

I would also thanks to Mr. Anoop K. Mathur, professor Suresh Garimella, professor Sugato Chakravarty and professor Athula Kulatunga for their help and guidelines in my Ph.D work.

TABLE OF CONTENTS

LIST OF TABLES

LIST OF FIGURES

ABSTRACT

Luo, Qi. Ph.D, Purdue University, May 2015. Control Oriented Concentrating Solar Power (CSP) Plant Model and its Applications. Major Professor: Kartik Ariyur, School of Mechanical Engineering.

Solar receivers in concentrating solar thermal power plants (CSP) undergo over 10,000 start-ups and shutdowns, and over 25,000 rapid rate of change in temperature on receivesr due to cloud transients resulting in performance degradation and material fatigue in their expected lifetime of over 30 years. The research proposes to develop a three-level controller that uses multi-input-multi-output (MIMO) control technology to minimize the effect of these disturbances, improve plant performance, and extend plant life. The controller can be readily installed on any vendor supplied state-of-the-art control hardware.

We propose a three-level controller architecture using multi-input-multi-output (MIMO) control for CSP plants that can be implemented on existing plants to improve performance, reliability, and extend the life of the plant. This architecture optimizes the performance on multiple time scalesreactive level (regulation to temperature set points), tactical level (adaptation of temperature set points), and strategic level (trading off fatigue life due to thermal cycling and current production). This controller unique to CSP plants operating at temperatures greater than 550 ^oC, will make CSPs competitive with conventional power plants and contribute significantly towards the Sunshot goal of 0.06/kWh(e), while responding with agility to both market dynamics and changes in solar irradiance such as due to passing clouds. Moreover, our development of control software with performance guarantees will avoid early stage failures and permit smooth grid integration of the CSP power plants. The proposed controller can be implemented with existing control hardware infrastructure with little or no additional equipment.

In the thesis, we demonstrate a dynamics model of CSP, of which different components are modelled with different time scales. We also show a real time control strategy of CSP control oriented model in steady state. Furthermore, we shown different controllers design for disturbance rejection and reference tracking to handle complex receiver dynamics under system disturbance and measurement noise. At last, we show different applications of this control oriented CSP model including life cycle enhancement and electricity load forecasting using both neural network and regression tree.

1. BACKGROUND AND MOTIVATION

1.1 Solar Energy Overview

According to technical report from National Renewable Energy Laboratory [1], solar energy technologies is still at unprecedented levels, with significant aids by the advent of utility-scale projects which sell their power directly to the utilities. These systems, compared with the traditional solar energy projects, can achieve significant economics of scale in operation, therefore reduce the cost of delivered power.

Based on database maintained by Solar Energy Industries Association [2], [3], there are around 16,043 megawatts(MW) of utility-scale solar resources under development within United States, of which photovoltaic(PV) projects make up 72% of the total project, and concentrating solar plant (CSP), which includes both CSP tower and CSP troughs, take 25% of the market share, as shown in figure 1.1.

1.2 CSP Tower Market and Technology Overview

CSP tower systems, often referred to as power towers or central receivers, are composed of four subsystems:

- Field of Heliostats.
- CSP receiver.
- Thermal storage.
- Steam turbine system.

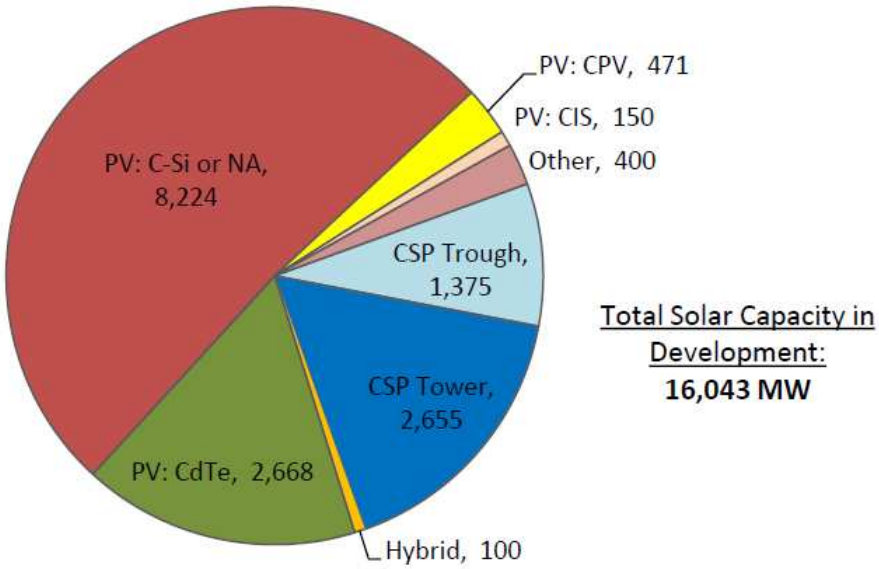

Figure 1.1. Total U.S. utility-scale solar capacity solar capacity under development (in MW) [1].

Upon operation, the field of heliostats will track the sunshine and redirect it to the receiver on top of a tower, the concentrated rate of the sunshine can usually be over 600 times, and therefore can heat transfer fluid (Usually steam, air, molten salt, etc.) up to 500 ^{o} to 850 ^{o}, the heated fluid will usually be used to serve as heat source of steam turbine, or to be stored in thermal storage system for further usage [4].

Of the total 1176 MW utility scale solar power under operation by January 2012, about 503 MW is by CSP facilities, and only 10 MW is by CSP tower [5], compared with 493 MW of CSP trough. However, the total capacity of CSP tower under development (2655 MW) is significant higher than the capacity of CSP trough under development (1375 MW), as shown in figure 1.2.

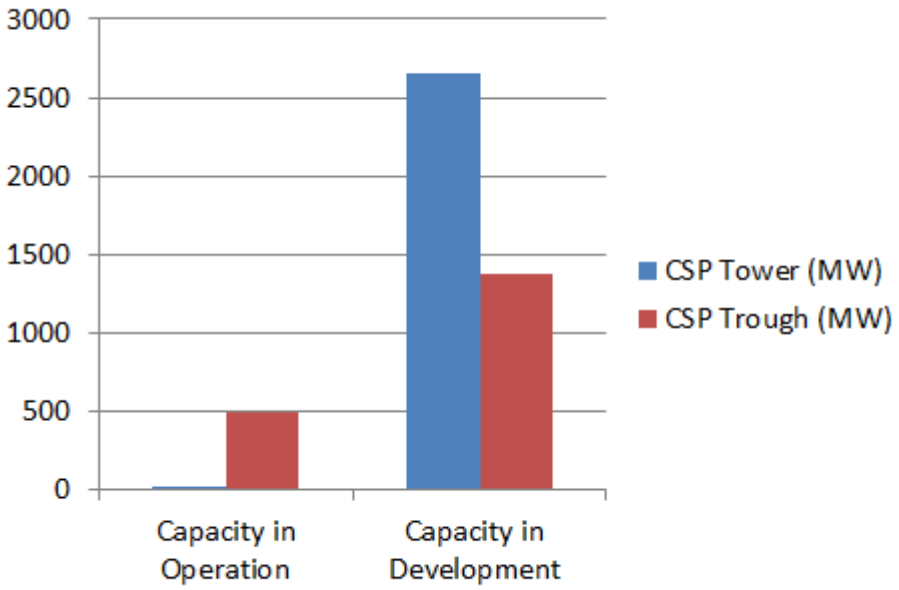

Figure 1.2. Capacity Comparison of CSP tower versus CSP trough as of January 2012(in MW) [6] [7].

1.3 Current CSP Control System Overview

In their expected lifetime of over 30 years, central receivers in solar power plants, undergo over 10,000 start-ups and shutdowns, and due to cloud transients undergo over 25,000 rapid changes in receiver metal temperature [8]. These changes are at least 25 to 50 times that of any conventional power plant. The metal temperatures range from ambient to over 700 ^oC on a daily basis during startups and shutdowns [9], and with transient clouds the solar irradiance can be reduced by 5% per second resulting in 600 ^oC per minute change in metal temperature at high flux points on the receiver [10]. These conditions cause significant thermal stresses in materials which reduce the lifetime of the plant and increase maintenance costs.

However, the problem with thermal stress is not apparent because observations are made on the heat transfer fluid temperature which does not fluctuate as rapidly as the metal temperature due to high thermal capacitance. These fluctuations in

fluid temperature are tolerated because they do not significantly impact performance and hence the open control strategies that to control heliostats and simple feedback control by manipulating flow rate to maintain heat transfer fluid temperature appear acceptable.

The fossil power plant industry knows that during every startup and shutdown process, the parts along hot fluid path suffer significant thermal cycling. The life cycle of those parts may be shorten due to the thermal cycling. This can result in a plant cost increase in two ways: First more parts have to be replaced during the inspections, which increase the plant maintenance cost. Second, since the parts maintenance cost get paid out earlier, this cost would have an additional cost increase due to the time value of money. Babcock & Wilcox study using BLESS code (boiler life evaluation and simulation system) and temperature vs time history of metal on headers showed that reducing the temperature imbalance in headers from 30^oC to 15^oC extends life by 3000 hours [11]. Prior control studies with solar central receiver showed that a different control strategy must be used during cloud transients. Further, this study found that the receiver flow patterns must be designed to include crossover from east to west side of receiver to minimize the temperature imbalance due to change in heat flux on these sides as the sun moves in the sky from east to west during the course of the day. These modifications are implemented in CSP systems that are being built. Grossman et al [12] developed correlations for the reduction in life time caused by creep-fatigue damage during thermal cycling.

1.4 Benefits and Motivation for New Multiple Input Multiple Output (MIMO) Controller

1. First Costs Reduction, Better Bankability, and Lower Levelized Energy Cost (LCOE).

   (a) Systems with simple controls are typically designed to run significantly below the maximum capability to avoid violating the maximum constraints

on temperatures or pressures. Advance control such as the proposed MIMO control, guarantee that these constraints are not violated, thus allowing the plant to operate closer to constraint boundaries and resulting in better output or efficiency point. For example, receiver fluid temperatures are designed to withstand temperatures of upto 600^oC but the maximum operating point is specified as 565^oC to allow for a safety margin. It is possible to increase this temperature to 580^oC with MIMO controller resulting in improving turbine generation efficiency by 1.1% and reducing first costs for the same rated capacity or improving energy output.

(b) With MIMO controller, we can better control the temperatures and rates of change of temperature. Material specifications and/or design safety factors can be relaxed, thus reducing first costs.

A trade-off between capital savings in (a) or (b) can be made.

2. Operating Cost Reduction

(a) With the proposed controller, thermal stress is explicitly controlled within specified limits. This will reduce metal fatigue and creep, fewer failures and better maintained assets which will result in reduced part replacement, improved availability, reduced maintenance costs and extended plant life. Reducing these costs impact the time it takes for the CSP system to reach profitability.

(b) With the proposed controller, market-decision making mechanism can be integrated with current CSP plant, increasing the automation in energy market biding and plant production planning.

2. CONTROL ORIENTED MODEL

As mentioned in chapter 1, the overall schematic of concentrating solar plant and corresponding control objective, as shown in figure 3.1, is composed of four parts:

2.1 Field of Heliostats

In the power tower system , the low dense solar radiation is reflected and concentrated over 500 times by a series of mirror called heliostats to the receiver of system, where the concentrated solar radiation can be absorbed and translated into thermal power to and used to generate electricity. The heliostat field is important subsystem because it is worth 50% of the total CSP system cost [13], and around 49% of the total system energy lost [14]. The control and optimization problems related to the subsystem are:

2.1.1 Location–Altitude,Azimuth Relation

The objective is to compute the sun position (zenith and azimuth angle at the observer location) as a function of the observer local time and position as discussed by Reda and Andreas [15], for calculation reference in heliostat field layout optimization and heliostat position control.

2.1.2 Field layout optimization

The significant factors affecting the performance of central receiver solar thermal systems including, (i) cosine losses, (ii) shading and blocking, (iii) receiver interception (i.e., heat not lost due to spillage), (iv) atmospheric attenuation between heliostat and receiver, and (v) heliostat reflectivity, as discussed in Schmitz et al's work [16].

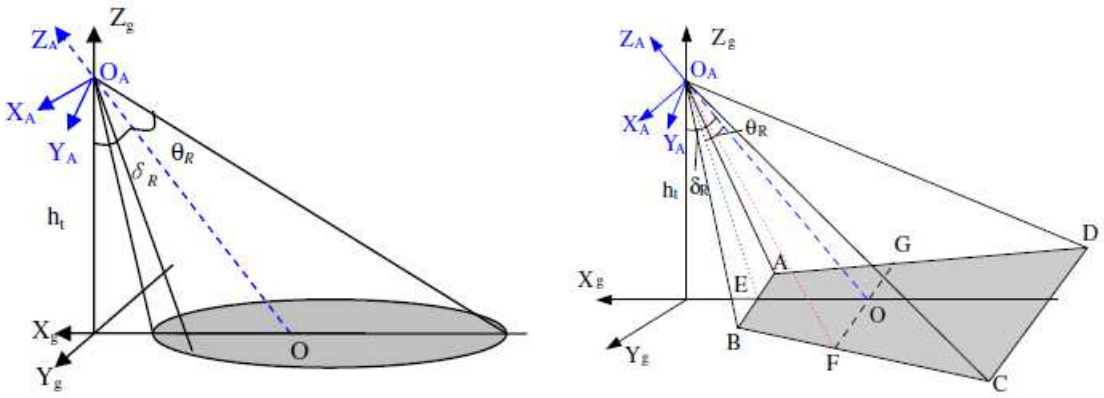

Figure 2.1. Heliostat field layout [17].

By setting the optimization objective function to be maximizing the efficiency, we developed field layout algorithm as described in equation:

$$\delta r = \frac{1}{2}(1.14424\cos(\theta_L - 1.0935 + 3.0684\theta_L - 1.1256\theta_L^2)HM \tag{2.1}$$

$$\delta az = (1.7491 + 0.6396\theta_L + \frac{0.02873}{\theta_L - 0.04902}) \cdot WM \cdot \frac{2r}{2r - HM * \delta r}(1 - \frac{HM \cdot \delta r}{2r \cdot THT}) \tag{2.2}$$

Equation (2.1) and (2.2) give the radius increment δr and angular increment δaz as shown in figure 2.2, where θ_L is the receiver aperture altitude angle with respect to a position on the ground (function of row radius), HM is the heliostat height, WM is the heliostat width, and THT is the tower height [18].

2.1.3 Heliostat tracking angle optimization

The objective is to build up functions relating four angular parameters in the altitudeazimuth tracking formulas: the tilt angle, Ψ_t, the tilt azimuth angle, Ψ_a, of the azimuth axis, the dual-axis non-orthogonal angle, τ_1 (bias angle of the altitude axis from the orthogonal to the azimuth axis), and the canting angle, μ, of the mirror

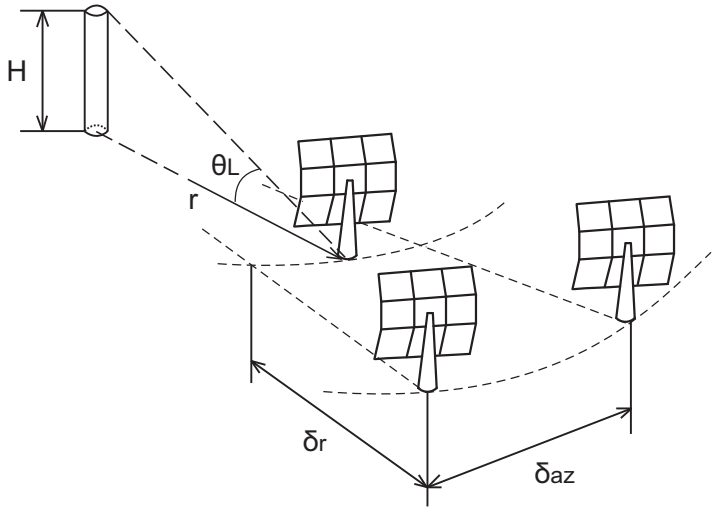

Figure 2.2. Heliostat field position [19].

surface plane relative to the altitude axis [20] as shown in figure 2.3 with the heat map distribution of the solar receiver.

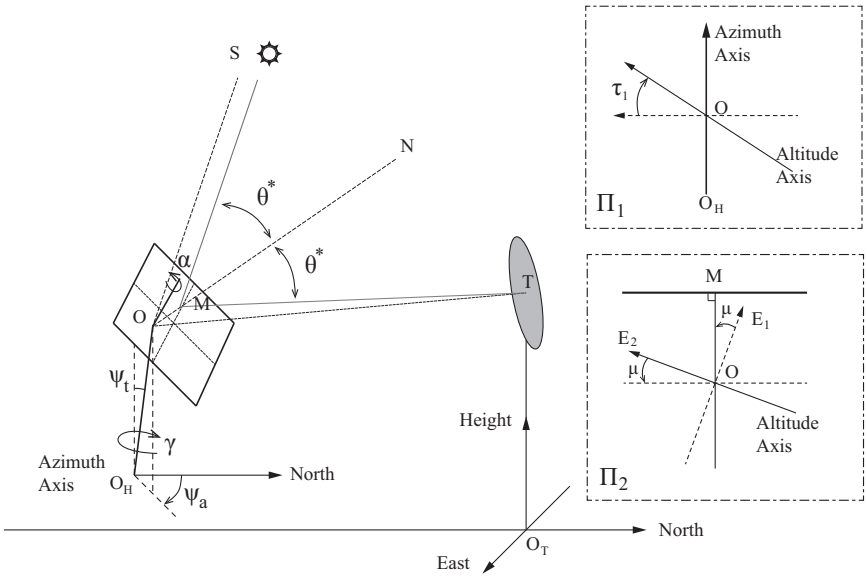

Figure 2.3. Altitude azimuth tracking geometry [21].

The mirror center nominal direction of heliostat as discussed in [22], can be expressed in [O;North-East-Height] coordinate system shown in figure 2.4 as:

$$\begin{aligned}\vec{n} &= (n_1, n_2, n_3) \\ &= (\cos\mu, \sin\mu, 0)(B_6 B_5 B_4 B_3 B_2 B_1)\end{aligned} \tag{2.3}$$

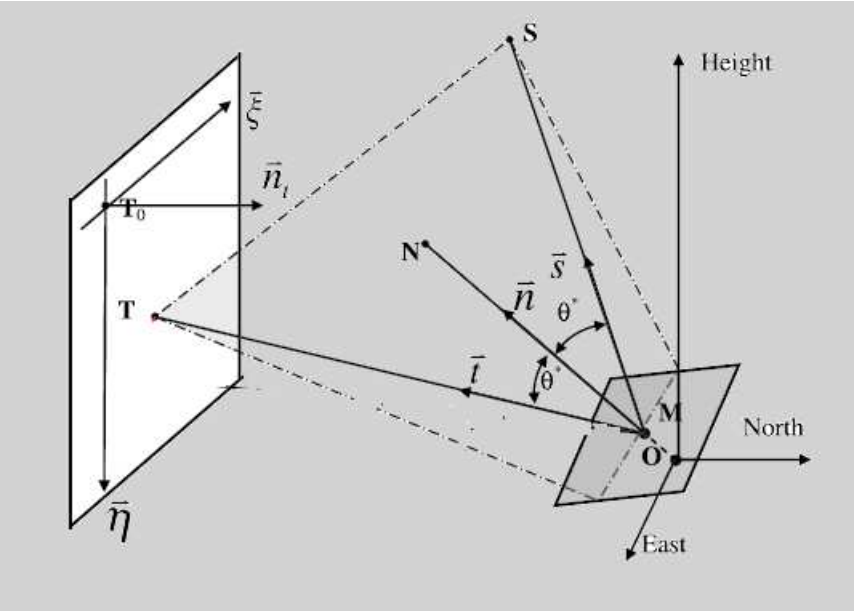

Figure 2.4. Intersection geometry of heliostat [19].

where $B_1 - B_6$ are rotational transformation matrices defined in Equation (2.4) to Equation (2.9)

$$B_1 = \begin{bmatrix} \cos\Psi_a & \sin\Psi_a & 0 \\ -\sin\Psi_a & \cos\Psi_a & 0 \\ 0 & 0 & 1 \end{bmatrix} \tag{2.4}$$

$$B_2 = \begin{bmatrix} \cos\Psi_t & 0 & -\sin\Psi_t \\ 0 & 1 & 0 \\ \sin\Psi_t & 0 & \cos\Psi_t \end{bmatrix} \tag{2.5}$$

$$B_3 = \begin{bmatrix} \cos\Psi_a & -\sin\Psi_a & 0 \\ \sin\Psi_a & \cos\Psi_a & 0 \\ 0 & 0 & 1 \end{bmatrix} \tag{2.6}$$

$$B_4 = \begin{bmatrix} \cos\gamma & \sin\gamma & 0 \\ -\sin\gamma & \cos\gamma & 0 \\ 0 & 0 & 1 \end{bmatrix} \tag{2.7}$$

$$B_5 = \begin{bmatrix} 1 & 0 & 0 \\ 0 & \cos\tau_1 & \sin\tau_1 \\ 0 & -\sin\tau_1 & \cos\tau_1 \end{bmatrix} \tag{2.8}$$

$$B_6 = \begin{bmatrix} 1 & 0 & 0 \\ 0 & \cos\tau_1 & \sin\tau_1 \\ 0 & -\sin\tau_1 & \cos\tau_1 \end{bmatrix} \tag{2.9}$$

Solar vector can be expressed as in Equation (2.10).

$$\vec{s} = (\cos\alpha\cos\gamma, \cos\alpha\sin\gamma, \sin\gamma) \tag{2.10}$$

where α is solar altitude angle, and γ is solar azimuth angle.

2.2 CSP Tower

CSP tower, or called CSP receiver, have been studies for years. The majority heat loss from receiver are from reflected radiation, emitted radiation, conduction and convection, as discussed in [23], and detailed heat loss analysis of various types of receivers with air, steam and molten salt as working fluid have also been discussed fully by researchers as well. [24], [25], [26],

2.2.1 CSP structural analysis

Solar image on the surface of the CSP receiver is usually symmetrical for one or two axis, depending on the heat map desired. Total heat transfer fluid (HTF) is usually separated into two geographically symmetrical and independent flow circuit.

The fluid flow dynamics would be arrange accordingly. The example we discuss is one-axis symmetrical along north-south direction, dividing the heat map of CSP receiver into east part and west part. In this scenario, we present CSP receiver flow arrangement of east part in figure 2.5. The direction of the flow, as shown in figure 2.5 and figure 2.6, is along: "Up header → 72 tubes → bottom header → 72 tubes → up header".

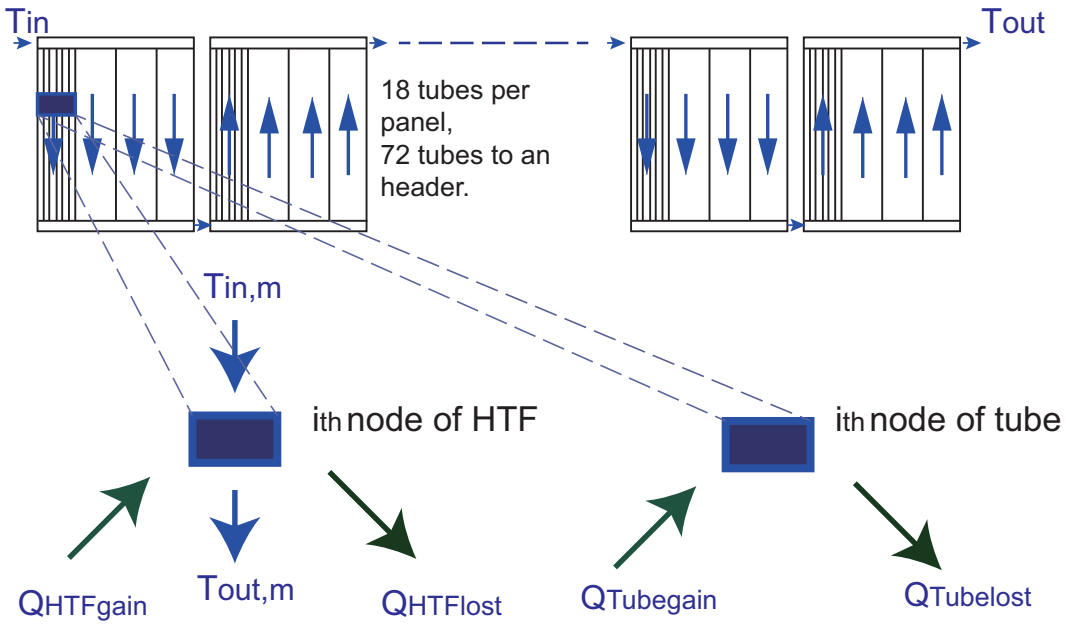

Figure 2.5. Flow path of working fluid inside CSP receiver.

2.2.2 CSP HTF dynamics

We divide the height of CSP into n segment, as shown in figure 2.7. The i^{th} segment is composed of two heat transfer processes: In the i^{th} node of tube, the heat transfer occurs between tube, ambient environment, and HTF; in the i^{th} node of HTF, the heat transfer occurs between tube and HTF. The heat transfer governing equations for segment i can be demonstrated from Equation (2.11)

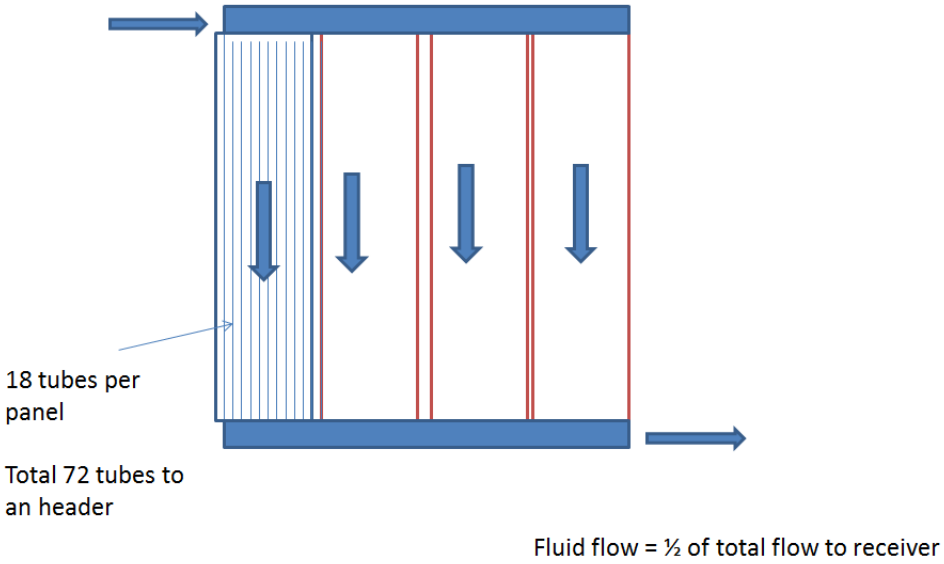

Figure 2.6. Panel Structure.

$$(mC_p)_{tube}\frac{dT_t(i,j,k)}{dt} = Q_{inc}(i,j,k) - (Q_{rad}(i,j,k) + Q_{conv}(i,j,k) + Q_{refl}(i,j,k)) - (UA)(T_t(i,j,k) - T_{HTF}(i,j,k)) \tag{2.11}$$

$$(mC_p)_{HTF}\frac{dT_{HTF}(i,j,k)}{dt} = (UA)(T_t(i,j,k) - T_{HTF}(i,j,k)) - Q_{HTF} \tag{2.12}$$

where $(mC_p)_{tube}$ is the mass times specific capacity of tube, $(mC_p)_{HTF}$ is the mass times specific heat capacity of working fluid, which are defined in Equation (2.13) and (2.14)

$$(mC_p)_{tube} = \pi \cdot d_{tube} \cdot 18 \cdot dz \cdot t_{tube} \cdot \rho_{tube} \cdot C_{Ptube} \tag{2.13}$$

$$(mC_p)_{HTF} = \pi \cdot d_{tube} \cdot 18 \cdot dz \cdot \rho_{HTF} \cdot C_{HTF} \tag{2.14}$$

$Q_{inc}(i,j,k)$ in Equation (2.11) is the energy absorbed due to incident of radiation reflected by the heliostat to i^{th} node on the j^{th} panel of k^{th} header on receiver.

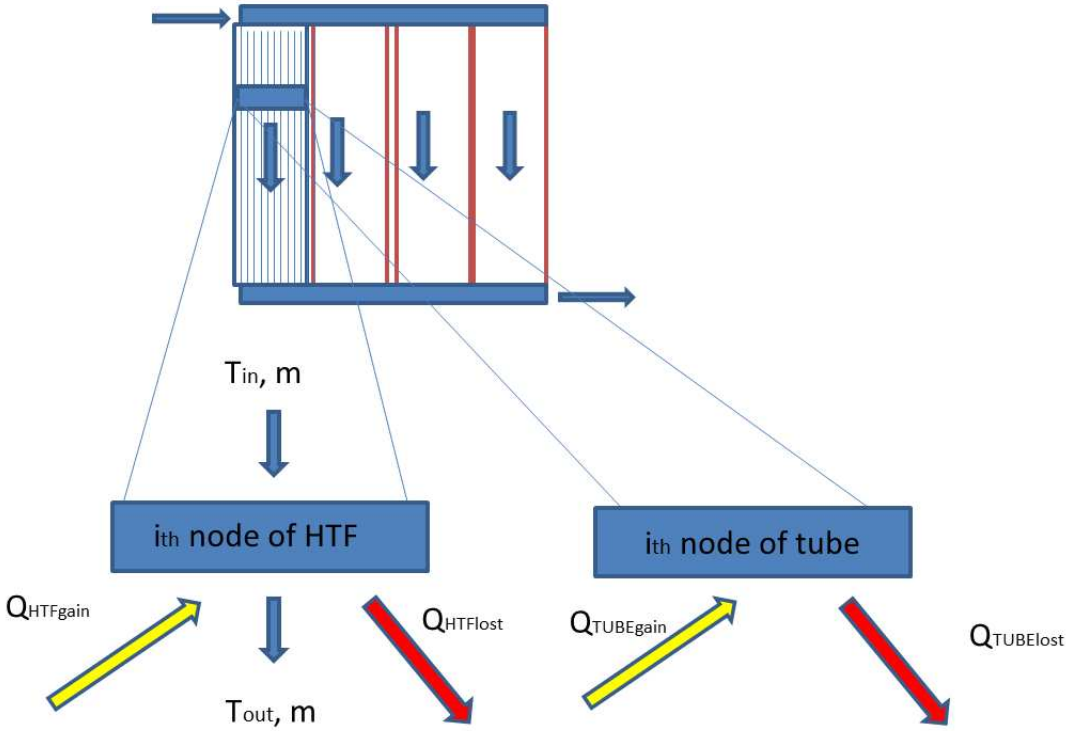

Figure 2.7. ith node micro-structure of panel.

U and A in Equation (2.11) and Equation (2.12) are convectional heat transfer coefficient between tube and HTF and surface area of the node respectively. U and A are defined in equation

$$U = U_0 \cdot (\frac{m_{HTF}}{m_{HTF}^{design}})^{0.8} \tag{2.15}$$

$$A = \pi \cdot d_{tube} \cdot dz \cdot 18 \tag{2.16}$$

$Q_{rad}(i,j,k)$, $Q_{conv}(i,j,k)$ and $Q_{refl}(i,j,k)$ are energy lost to ambient temperature due to radiation, convectional and reflection respectively, defined in Equation (2.17) to Equation (2.19).

$$Q_{rad}(i,j,k) = \sigma \cdot \epsilon \cdot f \cdot A \cdot (T_t^4(i,j,k) - T_{amb}^4) \tag{2.17}$$

$$Q_{conv}(i,j,k) = h_{conv} \cdot (T_t(i,j,k) - T_{amb}) \tag{2.18}$$

$$Q_{refl}(i,j,k) = 0 \tag{2.19}$$

σ in Equation (2.17) is StefanBoltzmann constant, ϵ is emissivity, f is radiation efficiency defined as $\frac{Q_{rad}^{tube}}{Q_{rad}^{blackbody}}$, T_{amb} is the ambient temperature. In Equation (2.18), h_{conv} is the convectional rate between tube and ambient temperature, here, loss due to reflection Q_{refl} is relatively small that we can reasonably approximate it to 0.

2.3 Thermal Storage

The output of a simple solar-only power plant depends largely on the solar input and weather condition, which, at most of the time, does not correspond with the utility load profile. In order to facilitate the output of solar station to minimize the weather influence, as well as to tail the plant output based on utility energy consumption patter, thermal storage system (TES) has largely be applied integrated in solar plants. By balancing the relationship between solar production and electricity load, we can improve power operation efficiency, reduce operational and management costs, and increase the stability of the system [27].

Thermal storage system usually use tank to store thermal energy. Inside the tank, the hot fluid is separated from the cold fluid by applying thermal gradient and heat transfer fluid (HTF) maintains high and low temperatures above and between the thermocline, respectively. Usually lower-cost filter material is used to displace high-cost fluid. [28]. There are two typical design options: two-tank storage, and single-tank thermocline storage [29]. In the single-tank system, cold fluid enters from the bottom, passes through CSP receiver and get heated, and eventually returns to

the top of the tank in the charging process. while in the discharing process, hot fluid is drawn from the top and pushed through a heat exchanger to get cooled. In a two-tank storage system, the molten-salt HTF flows from a cold tank to a hot tank through CSP receiver at charging, and flows back from the hot tank to cold though the steam generator at discharging cycle [30]. The advantage of single-tank system is that it is approximately 35% of the double-tank system of same capacity [31], but the latter has low-risk in energy storage since it separates the hot and cold fluid into two different tanks.

2.3.1 Thermal storage dynamics

The thermal storage dynamics equations has been developed by many researchers [32], [33], [34], and here we present dimensional governing equations for continuity, momentum and energy are presented in [29], it is worth to point out that, the thermal storage dynamics model in the paper are designed for CSP trough, but the model can be easily embedded into CSP tower system as well. Zhen Yang and Suresh V. Garimella's work had been presented and embedded in the overall CSP [27].

a. Continuity equation:

$$\varepsilon\frac{\partial\Phi_\rho}{\partial\tau}+\nabla\cdot(\Phi_\rho\mathbf{U})=0 \tag{2.20}$$

a. Momentum equation:

$$Re\frac{\partial\Phi_\rho}{\partial\tau}+Re\Psi\nabla\cdot(\frac{\Phi_\rho\mathbf{U}\mathbf{U}}{\varepsilon})=-\varepsilon\nabla P+\nabla\cdot\mathbf{T}+\varepsilon\Phi_\rho Gr\mathbf{e_x}-\varepsilon(\frac{\Psi_\mu\mathbf{U}}{Da^2}+\frac{FRe\Psi}{Da}\Phi_\rho\mathbf{U}\mathbf{U}) \tag{2.21}$$

c. Energy equation for the molten salt:

$$\begin{aligned}&PrRe\frac{\partial}{\partial\tau}(-\varepsilon\Phi_\rho\Phi_{Cpl}\Theta_l)+PrRe\nabla\cdot(\Phi_\rho\Phi_{Cpl}\Theta_l\mathbf{U})\\&=\frac{1}{\Psi}\nabla\cdot(\Phi_{ke}\nabla\Theta_l)+2PrARe\Phi_\mu[\mathbf{S}\mathbf{S}'+\mathbf{tr}(\mathbf{S})\mathbf{tr}(\mathbf{S}')]+\Phi_{kl}Nu_i\Psi(\Theta_s-\Theta_l)\end{aligned} \tag{2.22}$$

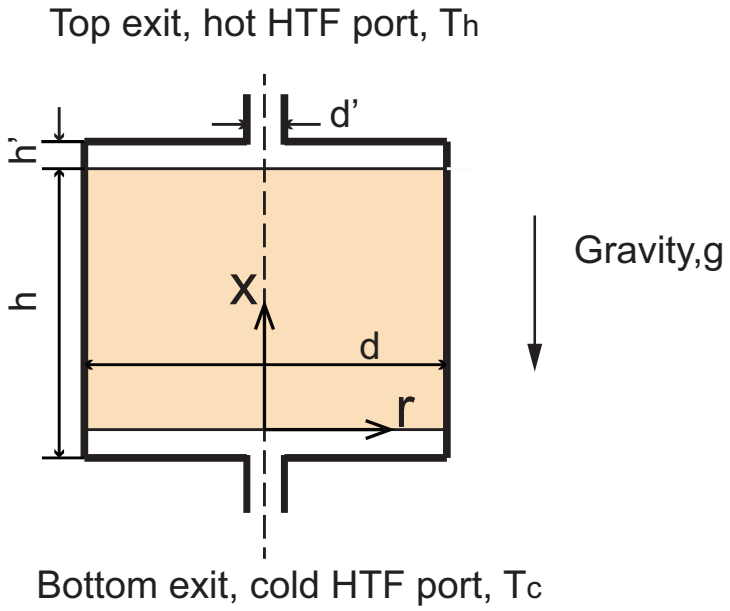

Figure 2.8. Schematic illustration of a TES thermocline, [27].

d. Energy equation for the filer material:

$$PrRe\frac{\partial}{\partial\tau}[(1-\varepsilon)\Omega\Phi_{\rho s}\Phi_{Cps}\Theta_s] = -\Phi_{kl}Nu_i\Psi(\Theta_s-\Theta_l) \tag{2.23}$$

with $\mathbf{T}$ and $\mathbf{S}$ defined in Equation (2.25).

$$\mathbf{T} = 2\mathbf{S} - \frac{2}{3}tr(\mathbf{S}) \tag{2.24}$$

$$\mathbf{S} = \frac{\nabla\mathbf{U} + (\nabla\mathbf{U})^T}{2} \tag{2.25}$$

Nusselt number Nu_i is approximated in [35] as in Equation (2.26), Ψ is defined as length ratio of the distance covered by the molten salt flow in a charge (or discharge) half-cycle to the diameter of the filler particles.

$$Nu_i = 6(1-\varepsilon)(2+1.1Re_L^{0.6}Pr_L^{1/3}) \tag{2.26}$$

The non-dimensional parameters included in Equations (2.20) and (2.23) are defined as in Equations (2.30) to (2.46):

$$\tau = \frac{tV_c}{d_s^2}, \tag{2.27}$$

$$X = \frac{x}{d_s}, \tag{2.28}$$

$$R = \frac{r}{d_s}, \tag{2.29}$$

$$\mathbf{U} = \frac{\mathbf{u}}{u_m}, \tag{2.30}$$

$$H = \frac{h}{d_s}, \tag{2.31}$$

$$D = \frac{d}{d_s}, \tag{2.32}$$

$$D' = \frac{d'}{d_s}, \tag{2.33}$$

$$Re = \frac{u_m d_s}{v_c}, \tag{2.34}$$

$$P = \frac{pd}{\mu_c u_m}, \tag{2.35}$$

$$Gr = \frac{g d_s^2}{v_c u_m}, \tag{2.36}$$

$$Da = \frac{\sqrt{K}}{d_s}, \tag{2.37}$$

$$A = \frac{u_m^2}{C_{plc}(T_h - T_c}), \tag{2.38}$$

$$Nu_i = \frac{h_i d_s^2}{k_{ls}}, \tag{2.39}$$

$$Pr = \frac{v_c}{\alpha_c}, \tag{2.40}$$

$$Pr = \frac{C_{Plc}\mu}{k_{lc}}, \tag{2.41}$$

$$\Theta_l = \frac{T_l - Tc}{T_h - T_c}, \tag{2.42}$$

$$\Theta_s = \frac{T_s - T_c}{T_h - T_c}, \tag{2.43}$$

$$\Omega = \frac{\rho_{sc} C_{Psc}}{\rho_{lc} C_{Pls}}, \tag{2.44}$$

$$\bar{\bar{T}} = \frac{\bar{\bar{\tau}} d_s}{\mu u_m}, \tag{2.45}$$

$$\nabla = \mathbf{e_x} \frac{\partial}{\partial X} + \mathbf{e}\cdot \frac{\partial}{\partial \theta} + \mathbf{e_r} \frac{\partial}{\partial R} \tag{2.46}$$

Coefficient Φ_ρ,Φ_{mu},Φ_{Cpl},Φ_{kl}, Φ_{ke}, $\Phi_{\rho s}$ and Φ_{Cps} represents the density, viscosity, specific heat, thermal conductivity, effective thermal conductivity, of molten salt, and density and specific heat of filter material, respectively, and expressed as in equation, and is fits nicely with data indicated in [36]

$$\Phi_\rho = 1 - \frac{0.732(T_h - T_c)}{2084.4 - 0.732 T_c} \Theta_I \tag{2.47}$$

$$\Phi_\mu = \frac{exp\{-4.343 - 2.0143 ln[(T_h - T_c)\Theta_I + T_c] + 10.094\}}{exp\{-4.343 - 0.20143 ln T_c + 10.094\}} \tag{2.48}$$

$$\Phi_{kl} = \frac{-6.52 \times 10^{-4}[(T_h - T_c)\Theta_l + T_c] + 0.5908}{-6.53 \times 10^{-4} T_c + 0.5908} \tag{2.49}$$

$$\Phi_{Cpl} = 1 \tag{2.50}$$

$$\Phi_{Cps} = 1 \tag{2.51}$$

$$\Phi_{\rho s} = 1 \tag{2.52}$$

$$\Phi_{ke} = \Phi_{kl} \frac{1 + 2\beta\phi + (2\beta^3 - 0.1\beta)\phi^2 + \phi^3 0.05 \exp 4.5\beta}{1 - \beta\theta} \tag{2.53}$$

where we have θ and β in Equation (2.53) defined as in Equation (2.55), as discussed in [37].

$$\theta = 1 - \varepsilon \tag{2.54}$$

$$\beta = \frac{k_s - k_l}{k_s + 2k_l} \tag{2.55}$$

Assume the inlet and outlet flow are of uniform temperature, with boundary condition defined as

- At the top exit of the filler bed in the discharge half-cycle when $(0 < \tau < 1)$:

$$\bar{U} = \bar{e_x} \tag{2.56}$$

$$\frac{\partial \Theta_l}{\partial X} = 0 \tag{2.57}$$

- At the top exit of the filler bed in the charge half-cycle when $(1 < \tau < 2)$:

$$\bar{U} = -\bar{e_x} \tag{2.58}$$

$$\Theta_l = 1 \tag{2.59}$$

- At the bottom exit of the filler bed in the discharge half-cycle when $(0 < \tau < 1)$:

$$\frac{\partial \bar{U}}{\partial X} = 0 \tag{2.60}$$

$$\Theta_l = 0 \tag{2.61}$$

- At the bottom exit of the filler bed in the charge half-cycle when $(1 < \tau < 2)$:

$$\frac{\partial \bar{U}}{\partial X} = 0 \tag{2.62}$$

$$\frac{\partial \Theta_l}{\partial X} = 0 \tag{2.63}$$

2.4 Steam Turbine Electricity Generation System

The steam turbines have been widely employed since almost one century ago to power generating due to their efficiencies and costs.

Figure 2.9 [1] gives a two level turbine electricity generation system, the high pressure steam comes from boiler, and is fed into turbine, in which it passes along the alternatively fixed and moving blades, from inlet port to outlet port, the cavity between blades and turbine are therefore increasing, causing a drop of steam pressure and an increase in kinetic energy of steam, the moving steam impacts on the rotational blades and transfer parts of its kinetic energy to these blades. The steam from outlet is fed into secondary turbine again, repeat the process, causing the drop of temperature and pressure of steam again. The outlet steam from the secondary turbine goes into condenser, in which the temperature of steam usually dropped below

[1]Figure source:"http://thermal-powerplant.blogspot.com/2010/06/steam-turbine-driven-electric-generator.html"

its boiling point, and fed into boiler again by passing through feedwater subsystem. Figure 2.10 [2] gives a temperature distribution of different processes.

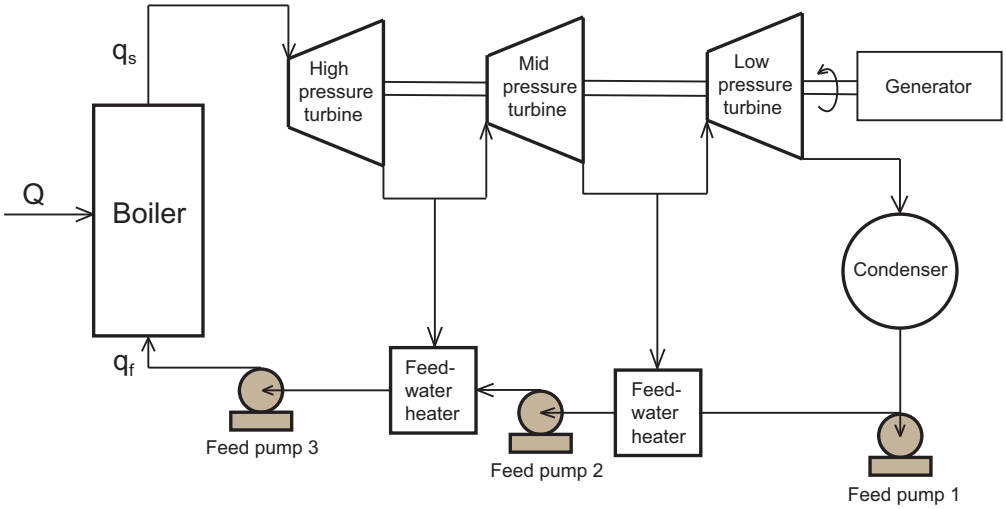

Figure 2.9. Schematic illustration of steam turbine power generation system.

Steam turbine of different levels of dynamic complexity have been modelled by different researchers [38], [39], [40], in this thesis, we divide steam turbine electricity generation system into different subsystems.

2.4.1 Boiler dynamics

A schematic picture of boiler system is shown in figure 2.11. The external heat, Q in the diagram is supplied by the thermal storage of CSP plant to the riser and heat up the working fluid (usually water). Feedwater, q_f, in the diagram is supplied to the drum and saturated steam, q_s is the heated steam flowing towards turbines. Inside the drum is a mix of saturated steam and liquid. It is worth to mention that as globally mass and energy balance need to be met during the whole process, and we assume that the heat transfer in the system is effective enough that all parts that the saturated steam-liquid mix are at thermal equilibrium.

[2]Figure source:"http://thermal-powerplant.blogspot.com/2010/06/steam-turbine-driven-electric-generator.html"

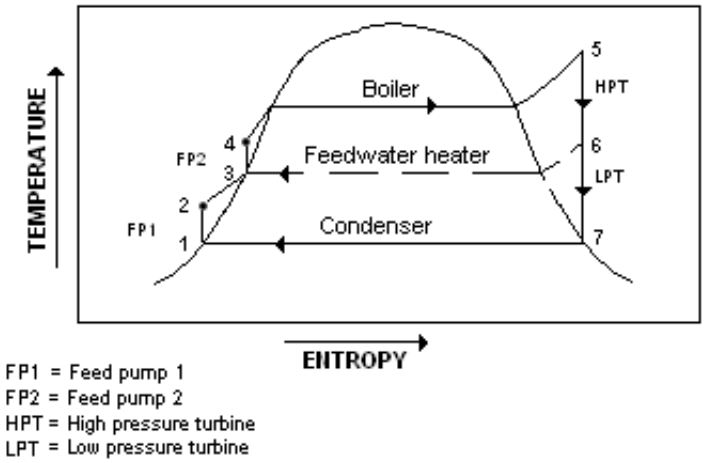

Figure 2.10. Schematic illustration of temperature distribution in steam turbine power generation system.

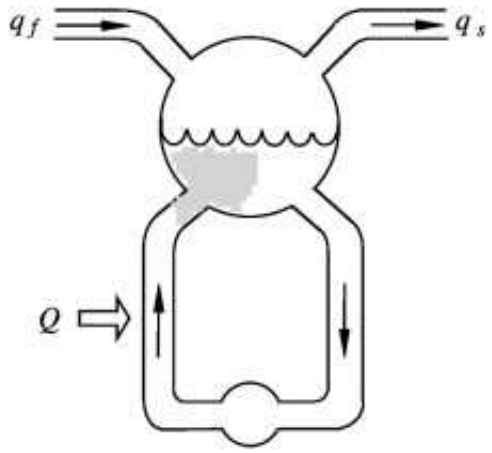

Figure 2.11. Schematic illustration of boiler system [41].

By choosing state variables:drum pressure p, total water volume V_{wt} steam quality at riser outlet α_r, and volume of steam under liquid level V_{sd}, we can derive dynamic Equations (refeqn:drum1) to (2.67), as shown in [41]:

$$e_{11}\frac{dV_{wt}}{dt} + e_{12}\frac{dp}{dt} = q_f - q_s \tag{2.64}$$

$$e_{21}\frac{dV_{wt}}{dt} + e_{22}\frac{dp}{dt} = Q + q_f h_f - q_s h_s \tag{2.65}$$

$$e_{32}\frac{dp}{dt} + e_{33}\frac{d\alpha_r}{dt} = Q - \alpha_r h_c q_{dc} \tag{2.66}$$

$$e_{42}\frac{dp}{dt} + e_{43}\frac{d\alpha}{dt} + e_{44}\frac{dV_{sd}}{dt} = \frac{\rho_s}{T_d}(V_{sd}^0 - V_{sd}) + \frac{h_f - h_w}{h_c}q_f \tag{2.67}$$

where we have

$$h_c = h_s - h_w \tag{2.68}$$

$$V_{st} = V_t - V_{wt} \tag{2.69}$$

$$e_{11} = \rho_w - \rho_s \tag{2.70}$$

$$e_{12} = V_{wt}\frac{\partial \rho_w}{\partial p} + V_{st}\frac{\partial \rho_s}{\partial p} \tag{2.71}$$

$$e_{21} = \rho_w h_w - \rho_s h_s \tag{2.72}$$

$$e_{22} = V_{wt}(h_w\frac{\partial \rho_w}{\partial p} + V_{st}(h_s\frac{\partial \rho_s}{\partial p} + \rho_s\frac{\partial h_s}{\partial p}) - V_t + m_t C_p\frac{\partial t_s}{\partial p} \tag{2.73}$$

$$\begin{aligned} e_{32} = {} & (\rho_w\frac{\partial h_w}{\partial p} - \alpha_r h_c\frac{\partial \rho_w}{\partial p})(1-\bar{\alpha}_v)V_r + (1-\alpha_r)h_c\frac{\partial \rho_s}{\partial p} + \rho_s\frac{\partial h_s}{\partial p})\bar{\alpha}_v V_r \\ & + (\rho_s + (\rho_w - \rho_s)\alpha_r)h_c V_r\frac{\partial \bar{\alpha}_v}{\partial p} \\ & - V_r \\ & + m_r C_p\frac{\partial t_s}{\partial p} \end{aligned} \tag{2.74}$$

$$e_{33} = ((1-\alpha_r)\rho_s + \alpha_r\rho_w)h_c V_r\frac{\partial \bar{\alpha}_v}{\partial \alpha_r} \tag{2.75}$$

$$\begin{aligned} e_{42} = {} & V_{sd}\frac{\partial \rho_s}{\partial p} + \frac{1}{h_c}(\rho_s V_{sd}\frac{\partial h_s}{\partial p} + \rho_w V_{wd}\frac{\partial h_w}{\partial p} - V_{sd} - V_{wd} + m_d C_p\frac{\partial t_s}{\partial p}) \\ & + \alpha_r(1+\beta)V_r(\bar{\alpha}_v\frac{\partial \rho_s}{\partial p} + (1 - \bar{\alpha}_v\frac{\partial \rho_w}{\partial p} + (\rho_s - \rho_w)\frac{\partial \bar{\alpha}_v}{\partial p}) \end{aligned} \tag{2.76}$$

$$e_{43} = \alpha_r(1+\beta)(\rho_s - \rho_w)V_r\frac{\partial \bar{\alpha}_v}{\partial \alpha_r} \tag{2.77}$$

$$e_{44} = \rho_s \tag{2.78}$$

where in Equation (2.64) to Equation (2.78), V denote the volume, ρ specific density, u specific internal energy, h specific enthalpy, t temperature, q mass flow rate, and subscripts s, w, f, and m refer to steam, water, feedwater and metal, double subscripts t denotes total system, d drum and r riser. $\bar{\alpha}_v$ and q_{dc} are given in Equation (2.79) and (2.80).

$$\bar{\alpha}_v = \frac{\rho_w}{\rho_w \rho_s}(1 - \frac{\rho_s}{(\rho_w - \rho_s)\alpha_r} ln(1 + \frac{\rho_w - \rho_s}{\rho_s}\alpha_r)) \tag{2.79}$$

$$q_{dc} = \sqrt{\frac{2\rho_w A_{dc}(\rho_w - \rho_s) g \bar{\alpha}_v V_r}{k}} \tag{2.80}$$

2.4.2 Steam turbine dynamics

Based on previous work done by Lin and Tsai [42], the steam turbine-generator unit has very complex mechanical characteristics. Here we can simplify the models to the lumped mass-damping-spring model shown in following equations:

$$J_{iB}\frac{d\omega_{iB}}{dt} = \tau_{iB} - D_{iB}\omega_{iB} - K_{iB}(\theta_{iB} - \theta_i) \tag{2.81}$$

$$i = H, M, L \tag{2.82}$$

The turbine rotor dynamics are as follows:

$$J_H\frac{d\omega_H}{dt} = \tau_H - D_H\omega_H - K_{HM}(\theta_H - \theta_M) - K_{HB}(\theta_H - \theta_{HB}) \tag{2.83}$$

$$J_M \frac{d\omega_M}{dt} = \tau_M - D_M\omega_M - K_{ML}(\theta_M - \theta_L) - K_{HM}(\theta_M - \theta_H) - K_{MB}(\theta_M - \theta_{MB}) \quad (2.84)$$

$$J_L \frac{d\omega_L}{dt} = \tau_L - D_L\omega_L - K_{LG}(\theta_L - \theta_G) - K_{ML}(\theta_L - \theta_M) - K_{LB}(\theta_L - \theta_{LB}) \quad (2.85)$$

The generator rotor dynamic equation is as follows

$$J_G \frac{d\omega_G}{dt} = \tau_{EM} - D_G\omega_G - K_{LG}(\theta_G - \theta_L) \quad (2.86)$$

The symbols J, K, D, T, v and u, respectively, represent the inertia constant, stiffness coefficient, damping coefficient, torque, angular velocity and angle. The subscripts H, M, L, G and B, respectively, represent high-pressure turbine rotor, mid-pressure turbine rotor, low-pressure turbine rotor, generator and blade. The τ_{EM} represents the electromagnetic torque of the generator.

2.4.3 Synchronous generator circuit model

The d-q dynamic model for three-phase windings and excitation windings, as discussed by Ewald and Mohammad [43], is shown in following equations:

$$v_{ds} = (\frac{\omega_r}{\omega_b}X_q)i_{qs} + (-r_s - \frac{p}{\omega b}X_d)i_{ds} + (\frac{p}{\omega_b}X_{md})i'_{fd} \quad (2.87)$$

$$v_{qs} = (-r_s - \frac{p}{\omega b}X_q)i_{qs} + (-\frac{\omega_r}{\omega_b}X_d)i_{ds} + (\frac{\omega_r}{\omega_b}X_{md})i'_{fd} \quad (2.88)$$

$$\tau_{EM} = (\frac{3}{2})(\frac{P}{2})[L_{md}i'_{fd}i_{qs}i_{ds} + (L_{mq} - L_{md})i_{qs}i_{ds}] \quad (2.89)$$

where P is the number of poles, v_{ds} is direct axis voltage, v_{qs} is quadrature axis voltage, v_r is mechanical angular velocity, v_b is rated system angular velocity, X_q is quadrature axis reactor, X_d is direct axis reactor, X_{md} is direct axis mutual reactor, i_{qs} is quadrature axis current, i_{ds} is direct axis current, i_{fd} is field current, r_s is stator resistance, L_{md} is direct axis mutual inductance, L_{mq} is quadrature axis mutual inductance.

3. REAL TIME CONTROL FOR STEADY STATE OPERATION

3.1 Three-level MIMO Controller Introduction

In order to address problem of creep-fatigue damage on the CSP receiver, as well as integrate market-decision control in the current CSP system. We propose three-level MIMO controller (referred to as the controller) that will build on previous work in model predictive and state feedback control and insights gained at Solar Two on effects of thermal cycling on creep-fatigue damage on receiver. The controller will explicitly take the rate-of-change of metal temperature and trade-off plant performance to help calculate the best control moves and minimize the burden on the operator diurnal startups and shutdowns and nominal cycling of loads.

The controller deals with the dynamics at different timescales - hours for market conditions to minutes for cloud transients and to seconds for metal temperature changes. For example, we propose to develop a MIMO controller with robust model matching and with full state estimation in real-time (seconds) to regulate temperature and thereby bound propagation of demand disturbances into the tactical control system; the tactical level adapts temperature set points (minutes) to minimize the propagation of solar irradiance uncertainties into strategic decision-making control. The strategic level (hours) in turn, trades off capital and production costs and suitably negotiates pricing with the grid operator. Table 3.1 gives a general operation time for gird control of different time scales, which, sets up a reactive time constrain in control of CSP. In particular, the milliseconds to seconds level simulations are important since:

- The milliseconds to seconds level model can capture the real time disturbance and transient system dynamics changes.
- With the captured system change, with the milliseconds to seconds level model, we can also analysis the how the transient disturbance and dynamics could be propagated to the tactical level (seconds to minutes level) and the strategy level (minutes to hours level).
- Based on the analysis of result (i.e. how the milliseconds level disturbance and dynamics change would affect the life time, system profit, etc.) We can adapt the milliseconds to seconds level control algorithm to minimize the error or disturbance propagated up.

The controller uses mathematical models of differing sophistication at each time-scale: non-linear distributed dynamic models for thermal stress cycling in the receiver, lumped nonlinear thermo-hydraulic models (for example, receiver thermal dynamics, drum boiler dynamics), semi-empirical models with parameter estimation for real-time control, empirical correlations to make strategic operating decisions via hedging/market algorithms.

3.2 State of Development of the Controller and Proposed Approach

The following is the starting point for this project:

- A multi state non-linear dynamic model of the solar central receiver.
- A lumped parameter model dynamic model of the power generation system including steam drum, superheater and molten salt loop dynamics.
- The control algorithms for the power block, thermal storage system, and cylindrical receiver.
- Baseline plant control structure, component dynamic models, and plant design point parameters.

Table 3.1. Grid Control Time Scales [44].

Action/Operation	*Time Frame*
Wave effects(fast dynamics, lighting-caused overvoltages)	Microseconds to milliseconds
Switching overvoltages	Milliseconds
Fault protection	100 ms
Electromagnetic effects in machine windings	Milliseconds to seconds
Stability	1 seconds
Stability augmentation	Seconds
Electromechanical effects of oscillations in motors & generators	Milliseconds to minutes
Tie line load frequency control	1-10 seconds, ongoing
Economic load dispatch	10 seconds-1 hour, ongoing
Thermodynamic changes from boiler control action	Seconds to hours
System structure monitoring	1 hr- 1 day
System state estimation	1-10 seconds
Security monitoring	1 minute to 1 hour
Load management, forecasting	1 hour to 1 day, ongoing
Maintenance scheduling	Months to 1 year, ongoing
Expansion planning	Years, ongoing
Power plant building	2-10 years, ongoing

- Sensors and actuators analysis, estimation of system measurement and disturbance range.
- Improved plant control algorithm for

Using the thermal stress models available in literature as a starting point we will design the model based predictive controller for the receiver and the entire plant. The design of the Controller includes several functional modules including system identification, state estimators, parameter estimators, adaptation mechanism and so on. Next, we will use thermal stress models and dynamic models with the Typical Meteorological Year (TMY) weather data and cloud passages from various directions and speed over the heliostat field for a location such as Daggett, California and

Table 3.2. List of targeted improvements.

Current Baseline control	*Issues with baseline controls*	*Targeted Improvement with proposed controller*
• PID control of temperature of HTF from receiver by manipulating flow rate , open loop control with heliostats for heat map adjustment, conventional power block and dispatch controls	• Fluctuations in HTF temperature. • Constraint on flow rates. • No closed loop control of receiver metal temperature resulting wide rate of change in metal temperature. • Periodic open loop adjustment of heliostat aiming. • Minimum coordination of receiver heat flux with load control.	• Reduced fluctuations in HTF temperature. • Managed rate of change of metal temperature by coordinating multiple manipulated variables. • Better management of heat rates by coordinating with thermal storage, adapted to changes in insolation and cloud transients.

show that stress or metal strain is reduced. To calculate the remaining life of the component, we will use correlations from published literature such as Babcock and Wilcox method [45] using BLESS models. The value of the life-extension will then be calculated using the amount of additional electricity generated and Sunshot specific cost of electricity [46] ($0.06 per kWh). A list of targeted improvements is shown in Table 3.2.

3.3 Technical Details of the Proposed Approach

We aim to automate control and optimization of the entire plant and provide specific guarantees for performance and safety at all time-scales of operation, integrate market prediction and manage the health of the system. These are illustrated in our control architecture schematic. This show the flows of matter, energy and information when the CSP is connected to the grid. To develop the controller, we will need valid mathematical models. Fortunately, several dynamic models of plant components are readily available. A few attempts were made to understand the effects of temperature excursions on material fatigue and material creep. These attempts at thermal stress models indicate that the allowable stress depends strongly on the rate of change of temperature, especially at high temperature points.

Figure 3.2 shows three scenarios: cycling, hot start and cold start. The MIMO controller has access to the full state and can handle all functions of it, and explicitly take into account in the control objectives, the time derivatives of metal temperature and uniformity of temperature. There are several control inputs, such as molten salt flow rate, molten salt input and output temperatures, steam and load conditions at the turbine generators, flow rate from the thermal storage system, aiming of heliostats that can be manipulated. Besides it can take into account factors which can be designed in, such as responsive drive systems to quickly manipulate tracking and aiming of few designated heliostats, a molten salt recirculation flow around the receiver, trim

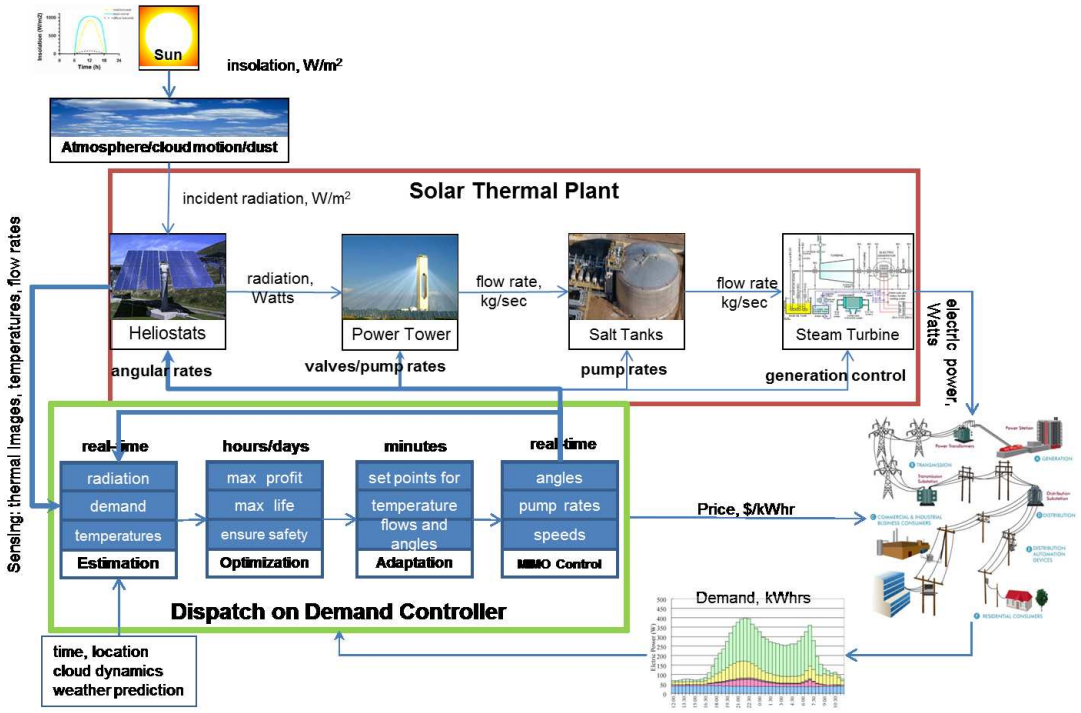

Figure 3.1. CSP Control Schematic.

variable speed pump to quickly manipulate flow rates. The effects and the value of these suggested changes in design of the CSP system will be evaluated.

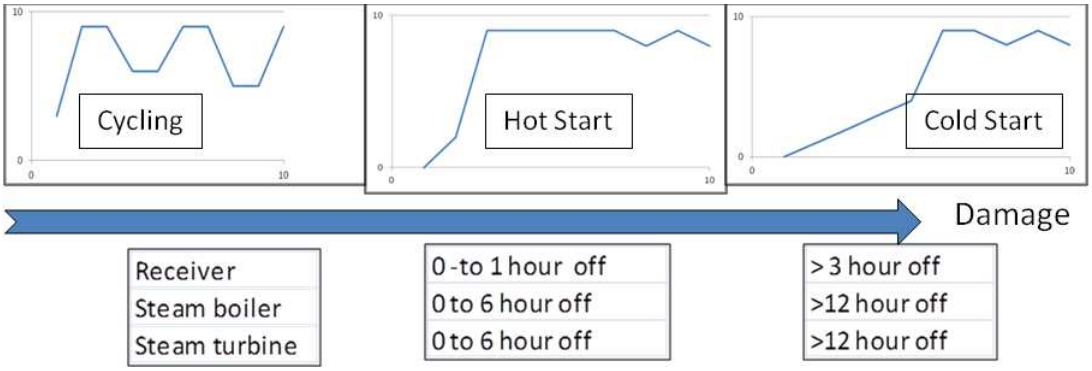

Figure 3.2. Typical CSP operation scenarios.

3.4 Controller Development

Our development is motivated by the structure of the model we have developed. We describe some of the non-standard steps needed to use well established linear control design methods for our purposes. These steps are needed for both estimation and control given the nonlinear dynamics of the power tower. The coupled equations that model heat transfer to each pipe segment in the power tower and the transfer of that energy to the high temperature fluid have a block strict-feedback structure, in that nonlinearities in the dynamics are accessible through a single integrator.

- State Estimation: We typically have measurements of flow temperature and can easily insert temperature sensors into the flow heads so each end of a tube in the power tower has a temperature measurement. The block strict feedback structure coupled with direct measurement of isolation, and flow rates permits design of state estimators similar to Kreisselmeier K-filters [47] or Marino-Tomei M-T filters [48] to estimate all temperature states.

- Parameter Estimation: The same parameterization used for the estimator above is also used for system identification via least squares techniques, of various physical parameters in the system that may differ from theoretical values and vary from time to time depending upon operating conditions and age of the plant. Our parameter estimation will run in batch mode so as to the lack of convergence guarantees arising from standard adaptive control methods [49].

- Block Feedback Linearization for cancelling nonlinearities: Radiation heat losses from the power tower tubes are strongly nonlinear; convection losses are also nonlinear. Because of the block strict feedback structure, we can directly cancel these nonlinearities [50], so that the system behaves linearly at any operating condition, and the rates of temperature change in the metal follow linear dynamics.

- Model Reference Control: We choose reference models with dynamics that optimize our cost functions over a period of time and drive the dynamics of the plant to these reference dynamics with our control inputssmall angular changes of the heliostats, pumping rates, and perhaps some valves.

- Set point adaptation: Because of uncertainties in the models we use, and due to changes in operating conditions, the plant will not follow the exact reference trajectory specified for it. To ameliorate these conditions, and send trajectory tracking to zero over the short term, we will use extremum seeking [51] to optimize the angle set-points to heliostats and temperature set points for fluid to optimize longer term cost functions. Set point adaptation via extremum seeking comes with exponential convergence guarantees, making it possible for us to incorporate this seamlessly into the longer time frame optimization.

- Long horizon optimization: Our objective is to form a cost function that incorporates the costs of thermal cycling of the power tower, mechanical cycling of the heliostats and pumps, along with the profits from the market over a one day time frame. We will use models of local climate, cloud movement, cloud tracking, and insolation to develop the overall cost function. This optimization will be performed through receding horizon methods using standard mathematical programming techniques.

- Recommendations for plant sensor placement/design alterations: Based on the performance of our controls on high fidelity simulation models, we will develop specifications for placing sensors to maximize the speed of plant control system response, and minimize its lifecycle costs. Design alterations such as the placement of additional valves or pumps will also be suggested.

These controllers can be implemented in any of the vendor supplied target hardware platforms. We expect to deliver functional software and demonstrate the controller using simulation of CSP operating under various operating modes .

3.5 Actuation Analysis

Actuation analysis is another important part in control and optimization design of concentrating solar plant. Actuators are devices which transform an electrical input signal into mechanical action or motion. Electrical motors, hydraulic pumps, relays are examples of actuators. In concentrating systems, possible actuators that might be used are electric motors with screw systems for heliostat position control and hydraulic pumps for molten salt fluid and steam fluid rate control. The specification of interest in our actuator selection includes:

- Electric motors
  - Speed range.
  - Accuracy.
  - Torque dynamic response.
  - Rated power.
  - Efficiency.
  - Load profile.
- Hydraulic pumps
  - Operating speed.
  - Operating temperature.
  - Operating horsepower
  - Maximum operating pressure.
  - Continuous operating pressure.
  - Maximum fluid viscosity.
  - Maximum fluid flow Displacement per revolution.
  - Speed-load characteristic equations.

A detailed comparison of electric motors and pumps are available in the appendix, the research objective is to build up input-output relationship between of actuators, especially the load profiles, which, will serve as constrains in final optimization functions.

Affect control time scale, affect the equilibrium mapping

3.6 Time Scale in the Simulation

Table 3.3. Ranges of system eigenvalues.

Action/Operation	*Time Frame (s)*
Receiver temperature change	$10^{-3} \sim 4 \times 10$
Receiver thermal strain calculation	$10^{-3} \sim 10^{-2}$
Receiver solar intensity adaptation	$1 \sim 10^{2}$
Boiler steam pressure change	$10 \sim 3 \times 10^{2}$
Thermal storage (6 hour)	$2 \times 10^{4} \sim 2 \times 10^{5}$
Steam turbine time constant	$10^{-1} \times 10$
Load/price forecasting	$10^{2} \sim 9 \times 10^{2}$

To ensure consistency and numerical stability of the overall simulation, its reproducibility, and for control design, we derived the time scales of all of the components. Given that the power tower and boiler are nonlinear, we only give the ranges of time constants of the components in the range of expected operating conditions. This architecture optimizes the performance on multiple time scales: reactive level (regulation to temperature set points), tactical level (adaptation of temperature set points), and strategic level (trading off fatigue life due to thermal cycling and current production). You can see that the time constants of the simulations results of different components are all within the time range of the components listed in table 3.3.

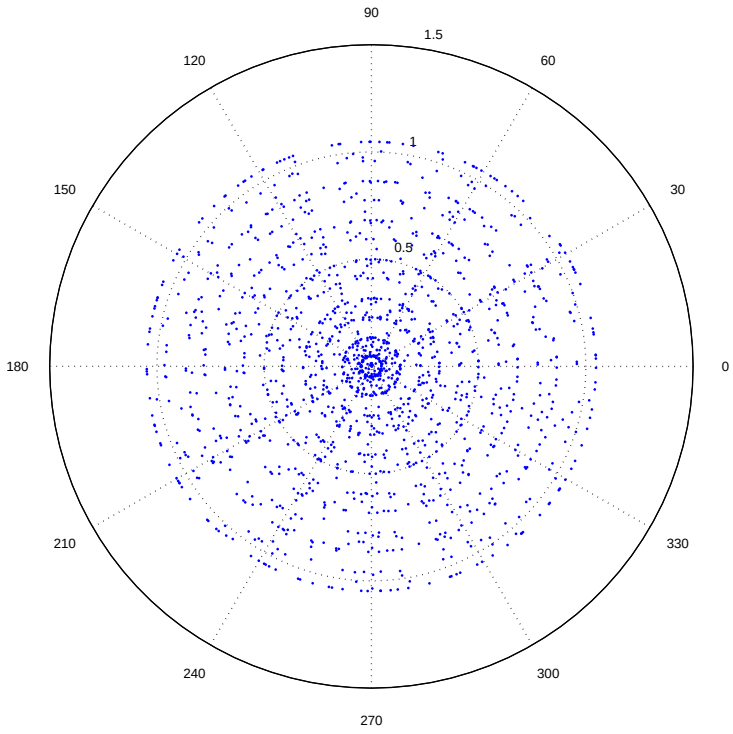

Figure 3.3. Optimized heliostat field position.

3.7 Heliostat Layout Optimization

Figure 3.3 shows the optimized heliostat layout. The parameters we are using in the simulation includes: Receiver height, $H = 18.8m$; heliostat height, $h = 5m$, width $w = 5m$, maximum radius $r_{max} = 110m$. The total number of heliostat in the figure is 1513.

3.8 Solar Tower Thermal Dynamics with LQR Control

In this section, we develop a control algorithm for a linearised model around equilibrium operation point, and build up tube life cycle - HTF flow rate relationship around the equilibrium point.

We design our output electricity power for the CSP system to be $100MW_e$, the calculated thermal power needed for this system would be $566.22MW_t$ based on System Advisor Model (SAM) provided by National Renewable Energy Laboratory [52]. Based on the thermal power needed, the receiver tower dimensions we choose are: Receiver height $H = 18.8m$, receiver diameter $D = 15.11m$, No. of headers $N = 16$ (8 headers on each of west & east side), with 4 panels/header and 18 tubes/panel. The tube dimensions are: tube outside diameter $D_{tube} = 0.04m$, tube thickness $t_{tube} = 0.00125m$. Other parameters in this test case includes HTF properties: HTF density $\rho_{HTF} = 1739kg/m^3$, specific heat capacity $C_{P,HTF} = 1529J/kg/K$, tube density $\rho_{tube} = 6400kg/m^3$ and tube specific heat capacity $C_{P,tube} = 500J/kg/K$. Maximum flow rate on each side $\dot{m}_{HTF} = 581.74kg/s$.

We take the east side of the tower in our analysis, and divide the thermal map into 8×8 nodes with energy balance analysis of each node shown as in figure 2.5. If we denote x_1, x_3, ..., x_{127} to be the HTF temperature of the 8×8 nodes, and x_2, x_4, ..., x_{128} to be the tube temperature of the 8×8 nodes, Equation (2.11) and Equation (2.12) can be rewritten in matrix form as in Equation (3.1) and Equation (3.2).

In these two equations, we have notations $A \sim E$ defined as $A = \frac{h_{tubes-HTF} * A_{tubes}}{C_{HTF}}$, $B = \frac{C_{P,HTF}}{C_{HTF}}$, $C = \frac{1}{C_{tubes}}$, $D = \frac{h_{tubes-env} * A_{tubes}}{C_{tubes}}$, $E = A + D$. u_1 is the control input 1 to the system representing the header flow rate in unit of kg/s, u_2 is the control input 2 to the system representing solar irradiation reflected by heliostats to each node in unit of W, d is the disturbance to the system representing ambient temperature in the unit of K. The subscript *tubes* represents the 72 tubes in the node of our interest, A_{tubes} is the surface area of the 72 tubes within one node. $h_{tubes-HTF}$ and $h_{tubes-env}$ is the heat transfer coefficient between tower and HTF, and heat transfer coefficient

between tower to environment respectively. C_{HTF} and C_{tubes} are of the unit of J/K and represent the thermal absorption ability of the HTF and tower respectively.

$$\begin{bmatrix} \dot{x}_1 \\ \dot{x}_2 \\ \dot{x}_3 \\ \dot{x}_4 \\ \vdots \\ \dot{x}_{127} \\ \dot{x}_{128} \end{bmatrix} = \begin{bmatrix} -(A+Bu_1) & A & 0 & 0 & \cdots & 0 & 0 & 0 & 0 \\ A & -E & 0 & 0 & \cdots & 0 & 0 & 0 & 0 \\ Bu_1 & 0 & -(A+Bu_1) & A & \cdots & 0 & 0 & 0 & 0 \\ 0 & 0 & A & -E & \cdots & 0 & 0 & 0 & 0 \\ \vdots & \vdots & \ddots & \vdots & & & & & \\ 0 & 0 & 0 & 0 & \cdots & Bu_1 & 0 & -(A+Bu_1) & A \\ 0 & 0 & 0 & 0 & \cdots & 0 & 0 & A & -E \end{bmatrix} \begin{bmatrix} x_1 \\ x_2 \\ x_3 \\ x_4 \\ \vdots \\ x_{127} \\ x_{128} \end{bmatrix} + \begin{bmatrix} 0 \\ Cu_2 \\ 0 \\ Cu_4 \\ \vdots \\ 0 \\ Cu_{128} \end{bmatrix} + \begin{bmatrix} 0 \\ D \\ 0 \\ D \\ \vdots \\ 0 \\ D \end{bmatrix} d + \begin{bmatrix} Bu_1 T_{inlet} \\ 0 \\ 0 \\ 0 \\ \vdots \\ 0 \\ 0 \end{bmatrix} \tag{3.1}$$

$$y = \begin{bmatrix} 0 & \cdots & 0 & 1 & 0 \end{bmatrix} \begin{bmatrix} x_1 \\ x_2 \\ x_3 \\ x_4 \\ \vdots \\ x_{127} \\ x_{128} \end{bmatrix} \tag{3.2}$$

The model has following characteristics:

- The model is non-linear due to the $-xu_1$ term.
- The model is a time variant system—The thermal properties of HTF including specific heat and conductivity would change as its temperature changes [53].

- The control input is limited: u_1 needs to be in the range of 0 to $586kg/s$, and u_2 needs to be in the range of 0 to I_{max} as well.

In this test case, we assume the solar irradiation on each node u_2 is constant and linearise the model around equilibrium point $u_1^*,\ x_1^*, \cdot, x_{128}^*$ in order to simplify the model for control design. Equations (3.1) and (3.2) can be rewritten as:

$$\begin{bmatrix} \delta\dot{x}_1 \\ \delta\dot{x}_2 \\ \delta\dot{x}_3 \\ \delta\dot{x}_4 \\ \vdots \\ \delta\dot{x}_{127} \\ \delta\dot{x}_{128} \end{bmatrix} = \begin{bmatrix} -(A+Bu_1^*) & A & 0 & 0 \\ A & -E & 0 & 0 \\ Bu_1^* & 0 & -(A+Bu_1^*) & A \\ 0 & 0 & A & -E \\ \vdots & \vdots & \vdots & \vdots \\ 0 & 0 & 0 & 0 \\ 0 & 0 & 0 & 0 \end{bmatrix}$$
$$\begin{bmatrix} \cdots & 0 & 0 & 0 & 0 \\ \cdots & 0 & 0 & 0 & 0 \\ \cdots & 0 & 0 & 0 & 0 \\ \cdots & 0 & 0 & 0 & 0 \\ \ddots & \vdots & \vdots & \vdots & \vdots \\ \cdots & Bu_1^* & 0 & -(A+Bu_1^*) & A \\ \cdots & 0 & 0 & A & -E \end{bmatrix} \begin{bmatrix} \delta x_1 \\ \delta x_2 \\ \delta x_3 \\ \delta x_4 \\ \vdots \\ \delta x_{127} \\ \delta x_{128} \end{bmatrix} + \begin{bmatrix} -Bx_1^* \\ 0 \\ Bx_1^* - Bx_3^* \\ 0 \\ \vdots \\ Bx_{127}^* - Bx_{128}^* \\ 0 \end{bmatrix} \delta u_1 \tag{3.3}$$

$$\delta y = \begin{bmatrix} 0 & \cdots & 0 & 1 & 0 \end{bmatrix} \begin{bmatrix} \delta x_1 \\ \delta x_2 \\ \delta x_3 \\ \delta x_4 \\ \vdots \\ \delta x_{127} \\ \delta x_{128} \end{bmatrix} \tag{3.4}$$

The equilibrium point $u_1^*,\ x_1^*, \cdot, x_{128}^*$ can be solved by setting $\dot{x}^* = 0$ in Equation (3.1) with boundary condition $x_1^* = 558.15K$ and $x_{127}^* = 847.15K$ as in design requirement, figure 3.4 gives a test case with $u_1^* = 458kg/s$. x axis represents nodes along receiver axial direction from top to bottom, y axis represents the nodes of east side of receiver along circular direction counter-clockwisely, z axis represents the nodes tube and HTF temperature in K. The surface with higher temperature represents the tube temperature of the nodes, while the one with lower temperature represents the HTF temperature of the nodes.

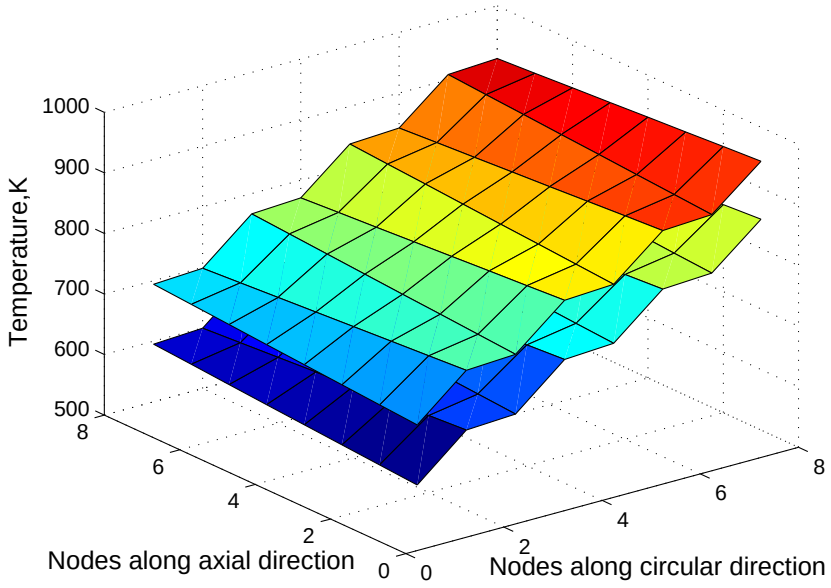

Figure 3.4. Equilibrium nodes tube and HTF temperature with $u_1^* = 450kg/s$.

In time $t \in [t_0, t_1]$, Equation (3.3) and (3.4) can be treated as linear time invariant system operating around equilibrium points. We apply Linear-quadratic regulator (LQR) [54] to this the model with quadratic cost function defined in Equation (3.5) The advantage of LQR controller over PID is that

$$J = \frac{1}{2}\delta x^T(t_1)F(t_1)\delta x(t_1) + \int_{t_0}^{t_1}(\delta x^T Q \delta x + \delta u^T R \delta u)dt \tag{3.5}$$

with control law $\delta u = -K\delta x$ and initial condition $\delta x(t_0) = \delta x^*$. $K = [k_1, k_2, ..., k_{128}]$ is the LQR gain. Here if we assume the temperatures of all nodes are observable, Equations above can be easily solved using standard numerical methods [55]. This assumption is valid since we can directly measure the temperatures of different nodes with a thermal camera.

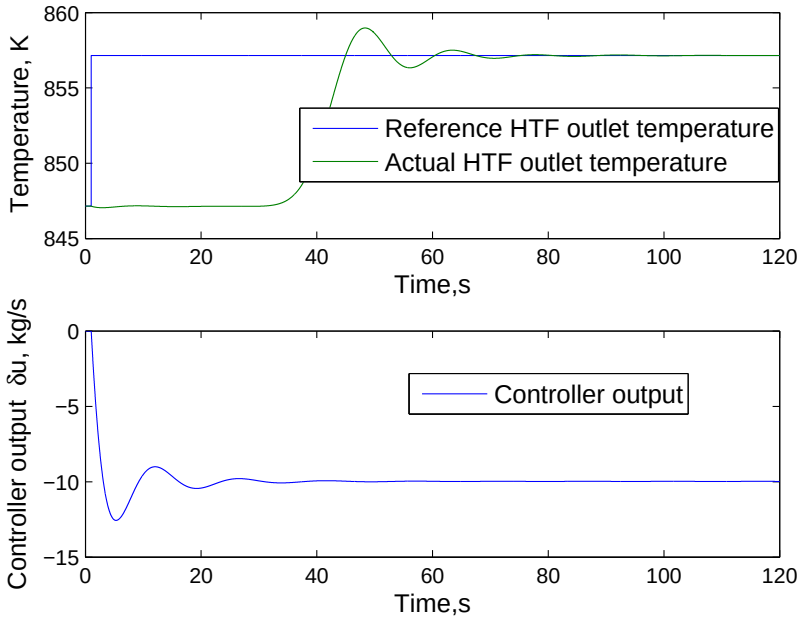

Figure 3.5. HTF outlet temperature and controller output with LQR.

Figures 3.5 and 3.6 give the simulation result for the LQR controlled receiver system with a $10K$ step signal in the reference HTF outlet temperature at $t = 1s$. In figure 3.5, x axis is simulation time in seconds, and y axis is the temperature of the tube or HTF in K. The first subplot gives the plot of the $10K$ step reference input to the system as well as the HTF outlet temperature (HTF temperature of node 64). It can be seen that there is about a $24s$ delay of actual HTF temperature rise compared to the reference input, this time delay is due to the travel time of the HTF inside the tube and this tells us the advance time needed to change reference input. The

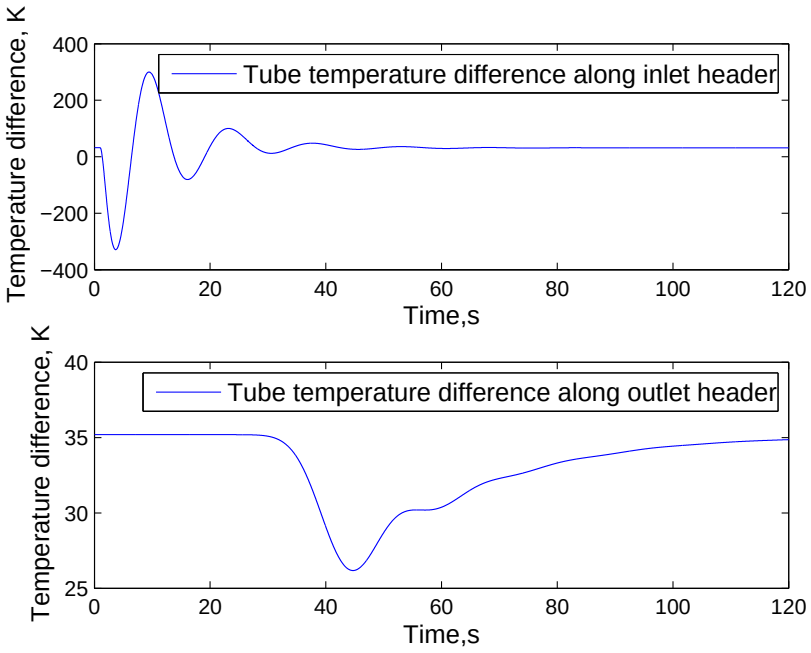

Figure 3.6. Receiver tube inlet temperature and outlet temperature with LQR.

second subplot of figure 3.5 gives the plot of controller output as a function of time $\delta u(t) = \sum_{i=1}^{128} -k_i \delta x_i(t)$.

Figure 3.6 gives the inlet header tube temperature and the outlet tube temperature difference. x axis is time is seconds, and y axis is temperature difference of the header in K. Since the receiver is divided into 8×8 nodes, the inlet header would contain node 1 to 8 and therefore its temperature difference would be $x_{16}^* + \delta x_{16} - x_2^* - \delta x_2$, similarly the outlet header difference is defined as the temperature difference of the last 8 nodes. This is important information since this header temperature difference relates to the header life cycle and therefore has a significant impact on the levelized cost of the plant, which we will discuss in more details in next section.

3.9 Receiver Temperature Equilibrium Map

In the longer time frame, the receiver temperature nonlinear dynamics model will vary as the model parameters such as HTF rate, solar intensity may vary.

In general, there are four sets of parameters that would affect the receiver outlet temperature:

1. HTF rate u_1.

2. Solar intensity concentrated on different nodes of receiver u_2,u_4,...u_{128}.

3. Ambient temperature d.

4. HTF inlet temperature T_{inlet}.

In previous section, the receiver dynamics has been linearised around equilibrium points u_1^*, $x_1^*, \cdot, x_{128}^*$. These equilibrium points are solved by setting $\dot{x}^* = 0$ in Equation (3.1) with boundary condition $x_1^* = T_{inlet} = 558.15K$ and $x_{127}^* = 847.15K$ from design requirement, HTF rate $u_1^* = 458kg/s$, solar intensity $u_2^* = u_4^* = ... = u_{128}^* = 950J/m^3$, ambient temperature $d^* = 25C$. Based on this equilibrium point, we derived LQR controller for receiver dynamics.

However, the LQR controller designed in previous section only works in the seconds to minutes duration or when the system operation point stays the same. In the minutes to hours time frame, the system operation points may change dramatically (Such as solar intensity), and we need to be able to design a controller whose parameters are variables of receiver operation point.

The pre-request of this parameter-varying controller design is to design a receiver temperature equilibrium map as a function of the four sets of parameters that listed above. The purpose of this map is to provide a operation point trajectory for the controller to follow when the receiver dynamics changes. The full map should be of 69 dimensions including: HTF rate, solar intensity reflected to 64 nodes on receiver, ambient temperature, HTF inlet temperature, and HTF outlet temperature.

The procedure of deriving this full map is to sweep through the 69 dimensional map up to the design constrains of each dimension (For instance, HTF rate can only vary between $0kg/s$ to $581.74kg/s$ according to the design constrain). Then validate if each set of 69 variables can lead the system to the equilibrium points that can meet both the design requirement for HTF temperature and receiver metal temperature.

Here we use a simple 2D map to help illustrate this idea further more: We assume HTF inlet temperature $T_{inlet} = 558.15K$, solar intensity $u_2 = u_4 = ... = u_{128}$, ambient temperature $d^* = 25C$, target HTF output temperature at equilibrium is $x^*_{127,target} = 847.15K$ from design requirement. We then sweep the combination of HTF rate and solar intensity on node (u_1, u_2) to find the receiver temperature equilibrium point.

The procedures are as follows:

1. Based on above constrains and receiver metal properties, derive the upper and lower receiver tube temperature limit.

2. Derive the HTF and receiver tube temperature distribution along nodes based on HTF inlet/outlet temperature equilibrium points and receiver tube temperature limit.– This result will serve as the initial condition in solving the receiver nonlinear dynamics equation.

3. Set $\dot{x} = 0$ in Equation (3.1) and solve this non-linear equation using the trust-region dogleg approach and initial conditions derived from previous step. HTF inlet temperature T_{inlet} stays the same in the process.

4. Form a set of candidate combinations (u_1, u_2) as shown in figure 3.7 by checking whether the HTF outlet temperature at equilibrium point is within the $\pm 5K$ of target HTF outlet temperature at equilibrium point $x^*_{127,target}$.

5. Narrow down the candidate set by checking that: With the candidate combinations (u_1, u_2), whether the receiver tube temperature exceeds its design limits from step 1.

3.10 Heat Storage

The heat storage thermal dynamics is complex, therefore we created look-up tables to describe the thermal dynamics during the charging-discharging process. From control point of view, we are more interested in the relationship between pump rate

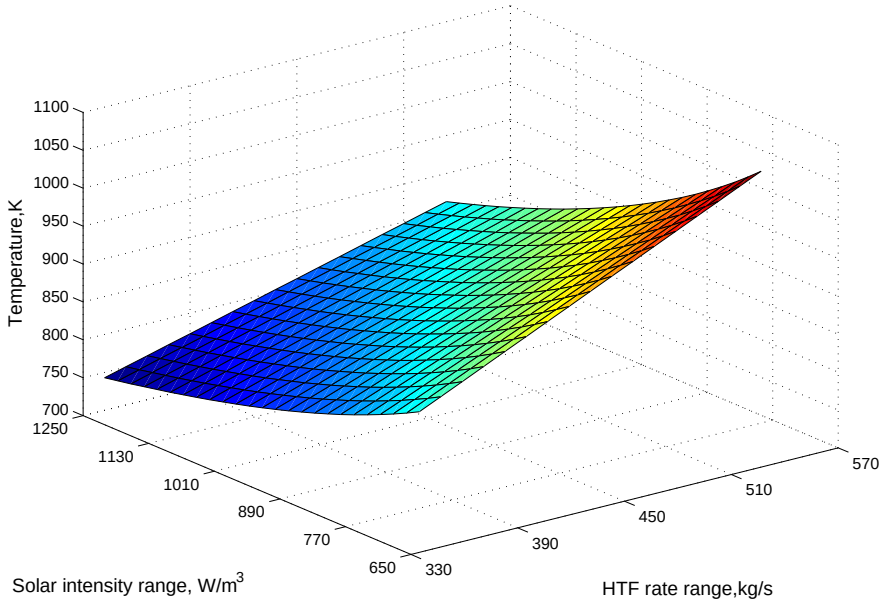

Figure 3.7. Equilibrium map candidate.

(which determines flow rate and Reynold number) the temperature of the inlet and outlet flow of solar thermal storage with different design dimensions. Therefore, instead of solving complex equations as shown in Equations (2.20) to (2.23), we use polynomial equations to approximate the charging and discharging process of thermal storage. Figure 3.8 gives the approximation result of the test case in [27] with $Re = 240, \Psi = 150$.

In our simulation model, we assume the storage is infinite. If the storage is finite, we will use first order system response to approximate the charging-discharging process. The procedures of doing that would be:

1. Develop the charging and discharging cycles simulation approximation for different Reynold number and flow rate.

2. In real time simulation, change the charging-discharging cycle approximations according to Reynold number and flow rate.

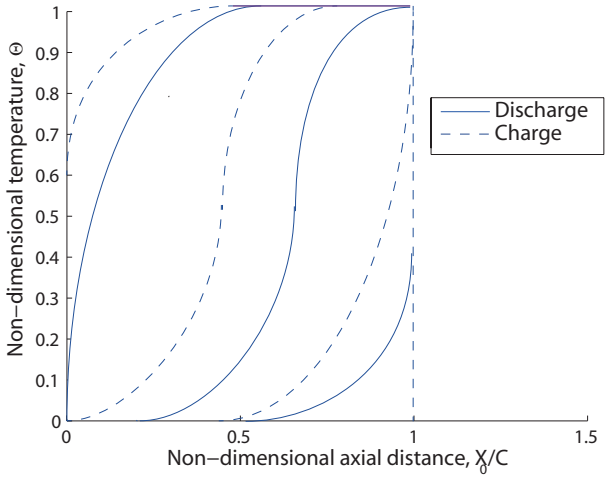

Figure 3.8. Discharge-charging cycle (Re = 240, $\Psi = 150$), $H = 1.0C_0$, [27].

3.11 Boiler Dynamics

Figure 3.9 gives the drum pressure for a step energy input Q from 0 to 10MW, with drum parameters: Volume of the drum $V_d = 40m^3$; Volume of the risers, $V_r = 37m^3$; Downcomer Volume, $V_{dc} = 11m^3$; Total volume of drum, downcomer, and risers, $V_t = V_d + V_r + V_dc$; Drum area at normal operating level, $A_d = 20$; Total metal mass $m_t = 300000kg$; Total mass of riser, $m_r = 160000kg$; Friction coefficient in downcomer-riser loop, k=25; empirical parameter in caculationg q_sd, $\beta = 0.3$, residence time of steam in drum, $T_d = 12s$; specific heat of metal, $C_p = 0.49$; area of downcomer, $A_{dc} = 10$; total drum mass, $m_d = m_t - m_r$; volume of steam under liquid level in the drum, $V_{0sd} = 15$.

The parameters including steam enthalpy, water enthalpy are updated via look-up table.

In figure 3.9, x axis for the three plots are time in seconds, y axis in the graph are drum pressure in MPa, total water volume in m^3, and the condensation water rate in kg/s, it needs to mention that since the steam out of the drum is constant, the drum pressure increases with a approximately constant rate, this increased pressure

improves the condensation rate of the water as well, and therefore cause a slight increase in the total water volume.

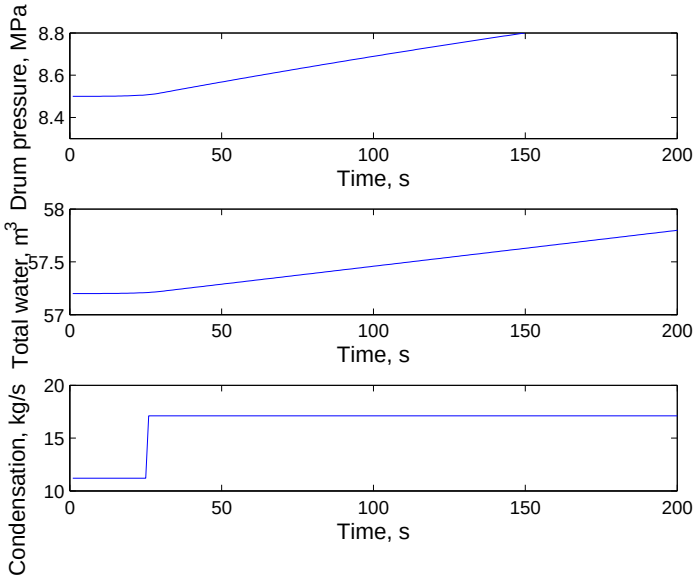

Figure 3.9. Drum pressure for constant flow rate and energy step input.

3.12 Control of Steam Turbine Generator Subsystem

The control methodology of steam turbine generator subsystem has been well developed by prior researchers [56].

We build up $per-unit(pu)$ synchronous generator with nominal power $600MVA$, line-to-line voltage $22kV$ and rotor speed to be $3600rpm$, and referenced output active power to be $566MW$ [57]. The mechanical power of the generator is provided by a three-stage steam turbine subsystem. In the turbine subsystem, the turbine torque fractions T as in Equations (2.82) to (2.86) are set to be $0.34, 0.33, 0.33$, stiffness coefficients K setted as $21.02, 42.7, 83.47$ (pu/rad) , damping factors D set as $0.08, 0.4, 2.4$ (pu of torque/pu of speed) as is in [58], and we further simply the system by setting the time constant of the turbine system to be $0.5, 3.3, 10(s)$.

The control algorithm for the steam turbine generator subsystem is shown in figure 3.10. The governor valve position in the subsystem is modelled as a first order system as in [59], with speed relay and motor time constants to be $0.001, 0.15(s)$ respectively. The gate opening limits are setted to be 0 to $4.5(pu)$ and its speed limits are setted to be -0.1 to $0.1(pu/s)$. In designing for the automatic generation controller for the subsystem, we assume zero dead zone and implement PID controller to the subsystem [60] with initial state starts from steady state:

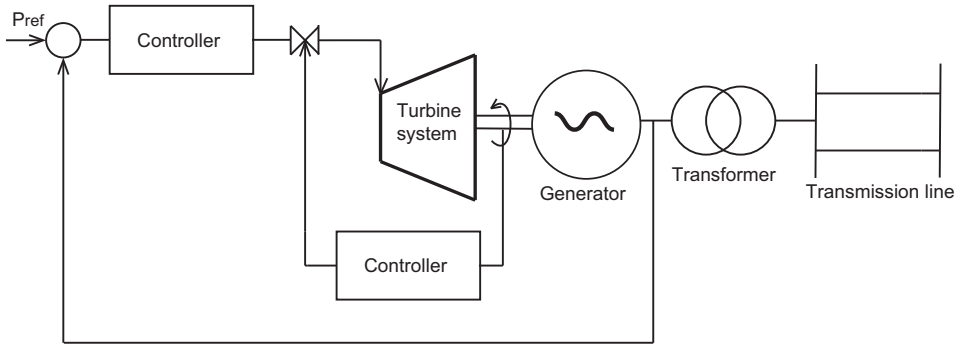

Figure 3.10. Control schematic for steam turbine generator system.

The simulation results with a step input of reference electricity generation P_{ref} at $0.01s$ are shown in figure 3.11 and figure 3.12. with the steam turbine generator subsystem connected with a $22kV$ to $500kV$ transformer and then to the transmission bus line. In figure 3.11, the first sub-plot shows the reference output active power and actual active output power, the second sub-plot shows the mechanical power input to the generator from the steam turbine system. The X axis on both sub-plots are time in s, Y axis are power in pu. Figure 3.12 gives the speed deviation of the three turbines and generator with respect to nominal value in the first sub-plot and the torques between three turbines and the turbine-generator system in the second sub-plot. The X axis in both sub-plots are time in s, Y axis in the first sub-plot is speed in pu, and in the second is torque in pu. We can see from the two plots that

with our speed governor and controller design, the active power falls within the 2% steady state error range in less than $0.3s$ with maximum overshoot to be $-1pu$.

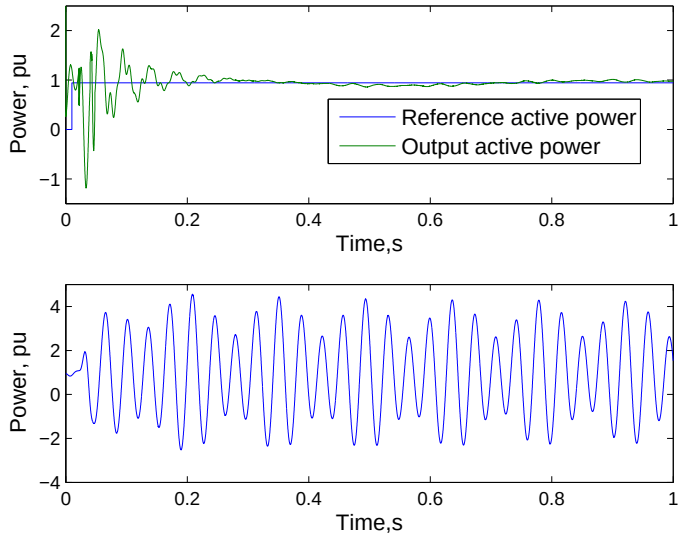

Figure 3.11. Output active power from generator and mechanical power input to the steam turbine generator system with controllers in pu.

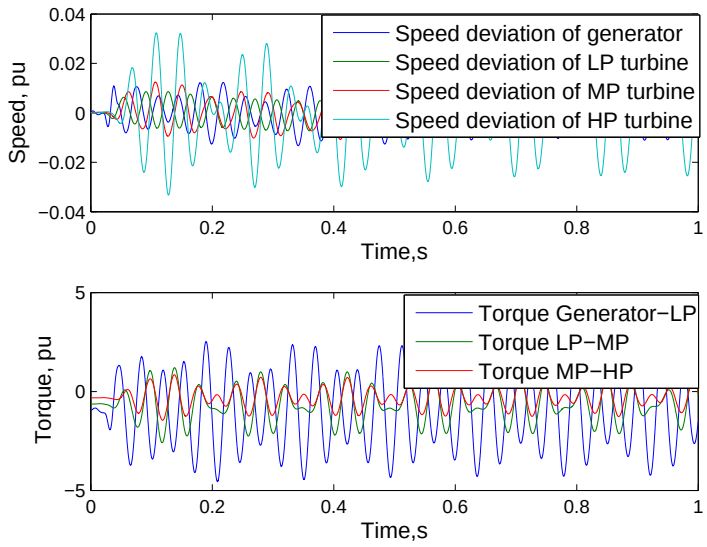

Figure 3.12. Speed deviation for the turbines and generator and torques between turbines-generator.

4. CONTROLS WITH SMALL DISTURBANCE

4.1 Sensing and State Estimation

As stated in previous chapter, sensing and state estimation is essential in solar concentrating plant optimization in order to have full state observability and controllability of whole system.

- Measurement and estimation of solar altitude angle α_s and solar azimuth angle γ_s and solar intensity I at time t and t+1 respectively.
- Measurement and estimation of tile angle Ψ_t, tile azimuth angle Psi_a, bias angle of altitude axis from the orthogonal of azimuth axis τ_1 and canting angle μ of the altitude-azimuth tacking geometry of heliostats at time t and t+1 respectively.
- Measurement and estimation of ambient temperature T_{amb}, tube temperature and HTF temperature $T_{tube}(i,j,k)$, $T_{HTF}(i,j,k)$ of the ith nodes on the jth header of panel k in the receiver subsystem at time t and t+1 respectively.
- Measurement and estimation of axial temperature from hot molten salt temperature T_h to cold salt temperature T_l for both charging and discharging processes at time t and t+1 respectively.
- Measurement and estimation of boiler input power Q, inlet volume and outlet steam flow rate and steam temperature q_f, q_s, T_f, T_s, drum pressure p_{drum}, volume of steam under liquid level in the drum V_sd at time t and t+1 respectively.

- Measurement and estimation of the pressure in electricity generator p_{HP} and p_{LH} in HP-turbine and in LP-turbine, as well as the steam temperature T_{HP}, T_{LP}, steam flow rate q_{HP}, q_{LP} at time t and t+1 respectively.

- Measurement and estimation of electricity demands and prices in both day ahead electricity markets and real time electricity markets D_{DA}, D_{RT}, p_{DA}, p_{RT} at time t and t+1 respectively.

A general introduction of sensing technology in usage is in the appendix. In the following objective, in each of the sensor we are going to use, the following characters are needed for system design and :

- Input resolution.
- Output resolution.
- Input range.
- Output range.
- Maximum non-linearity.
- Maximum hysteresis.
- Reaction time.

4.2 Receiver Dynamics Model with Measurement Error and State Disturbance

We are building a three-level controller architecture using multi-input-multi-output (MIMO) control for CSP plants that can be implemented on existing plants to improve performance, reliability, and extend the life of the plant as described in previous sections. This architecture optimizes the performance on multiple time scales reactive level (regulation to temperature set points), tactical level (adaptation of temperature

set points), and strategic level (trading off fatigue life due to thermal cycling and current production).

We first focus on the reactive level, since the time scale of this one is from milliseconds to minutes level, we can assume that the solar irradiation during this time interval would be constant and therefore the major system disturbance is from ambient temperature, if we are going to be developing the disturbance rejection model for the system, Equations (3.3) and (3.4) can be rewritten as:

$$
\begin{bmatrix} \delta\dot{x}_1 \\ \delta\dot{x}_2 \\ \delta\dot{x}_3 \\ \delta\dot{x}_4 \\ \vdots \\ \delta\dot{x}_{127} \\ \delta\dot{x}_{128} \end{bmatrix} = \begin{bmatrix} -(A+Bu_1^*) & A & 0 & 0 \\ A & -E & 0 & 0 \\ Bu_1^* & 0 & -(A+Bu_1^*) & A \\ 0 & 0 & A & -E \\ \vdots & \vdots & \vdots & \vdots \\ 0 & 0 & 0 & 0 \\ 0 & 0 & 0 & 0 \end{bmatrix} \begin{bmatrix} \cdots & 0 & 0 & 0 & 0 \\ \cdots & 0 & 0 & 0 & 0 \\ \cdots & 0 & 0 & 0 & 0 \\ \cdots & 0 & 0 & 0 & 0 \\ \ddots & \vdots & \vdots & \vdots & \vdots \\ \cdots & Bu_1^* & 0 & -(A+Bu_1^*) & A \\ \cdots & 0 & 0 & A & -E \end{bmatrix} \begin{bmatrix} \delta x_1 \\ \delta x_2 \\ \delta x_3 \\ \delta x_4 \\ \vdots \\ \delta x_{127} \\ \delta x_{128} \end{bmatrix} + \begin{bmatrix} -Bx_1^* \\ 0 \\ Bx_1^* - Bx_3^* \\ 0 \\ \vdots \\ Bx_{127}^* - Bx_{128}^* \\ 0 \end{bmatrix} \delta u_1 + \begin{bmatrix} 0 & 0 \\ C & D \\ 0 & 0 \\ C & D \\ \vdots & \\ 0 & D \\ C & D \end{bmatrix} \begin{bmatrix} \delta u_2 & \delta d \end{bmatrix} \tag{4.1}
$$

$$\delta y = \begin{bmatrix} 0 & \cdots & 0 & 1 & 0 \end{bmatrix} \begin{bmatrix} \delta x_1 \\ \delta x_2 \\ \delta x_3 \\ \delta x_4 \\ \vdots \\ \delta x_{127} \\ \delta x_{128} \end{bmatrix} + \delta v \tag{4.2}$$

In Equation (4.1) and (4.2), $\begin{bmatrix} \delta u_2 & \delta d \end{bmatrix}$ in this equation represents the fluctuation of solar intensity and ambient temperature around equilibrium point u_2^* and d^*. Also, δv in this equation is representing the noise introduced by the measurement system.

In the real world scenario, the we would be facing the following challenges in controller design:

1. The solar intensity and ambient temperature can be a constant perturbation to the system, and even on seconds level, these two values can be changing dramatically between two consecutive sample periods.

2. The node temperatures from thermal camera would be of measurement error. This is specially challenging when the measurement noise level is comparable with the reference input to the system. i. e. The measurement is $\pm 5C^o$, while our control objective is to increase the receiver outlet temperature by $5C^o$ as well.

We design two different Linear-Quadratic-Gaussian (LQG) controllers to concur problems above: LQG regulation, which is a combination of LQR and Kalman filter, for disturbance rejection; LQG servo controller, which is a combination of Linear-Quadratic-Integrator (LQI) and Kalman filter, for reference tracking problem.

4.3 Kalman Filter Design

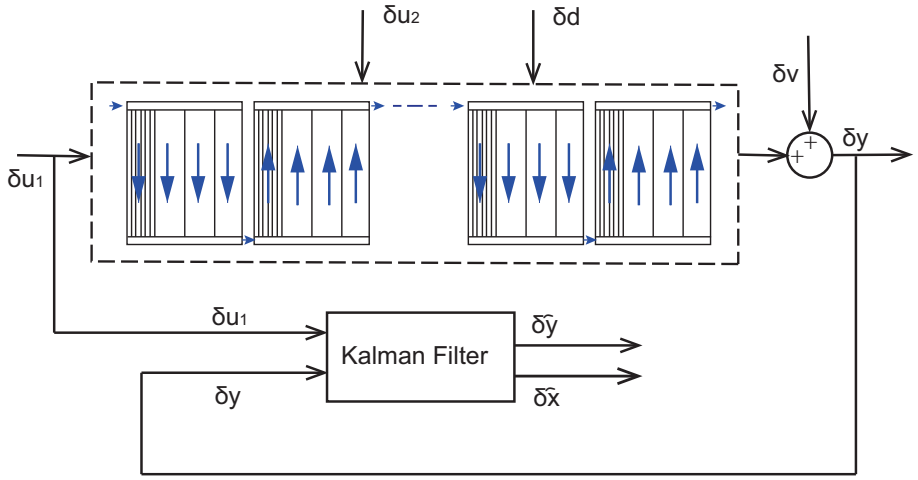

Figure 4.1. Kalman filter schematic for receiver dynamics with small disturbance

Figure 4.1 gives the schematic of Kalman filter design for receiver dynamics with small disturbance. The block "Kest" represents the Kalman filter estimation of system described by Equation (4.1). The Kalman filter would be updated in milliseconds to seconds level, with this execution time interval, the following assumption holds:

1. In the milliseconds to seconds level, fluctuation of solar intensity δu_2, fluctuation of ambient temperature δd can be interpreted as Gaussian white noise around equilibrim point u_2^* and d^* respectively. The measurement noise δv in this level is also Gaussian white noise. Therefore we would have $E(\delta u_2) = E(\delta d) = E(\delta v) = 0$.

2. The auto correlation and cross correlation of the three variables would be

$$Q_n = E(\begin{bmatrix}\delta u_2 & \delta d\end{bmatrix}\begin{bmatrix}\delta u_2^T \\ \delta d^T\end{bmatrix}) \tag{4.3}$$
$$= E(\delta u_2 \delta u_2^T + \delta u_2 \delta d^T + \delta d \delta u_2^T + \delta d \delta d^T)$$

$$R_n = E(\delta v \delta v^T) \tag{4.4}$$

$$N_n = E(\begin{bmatrix}\delta u_2 & \delta d\end{bmatrix}\delta v^T) \tag{4.5}$$

3. The Kalman filter can be designed as steady state Kalman filter, since we can safely assume that the above covariances are constant during milliseconds to seconds level control. — This assumption is not true in seconds to minutes level control, during which we should design time varying Kalman filter instead.

4. The Kalman filter we design would be current estimator, where we generates output estimates $\delta\hat{y}[n|n]$ (Estimate of HTF temperature difference at receiver outlet, δx_{127} at time interval n.) and state estimates $\delta\hat{x}[n|n]$ (Estimate of all HTF temperature difference and all tube temperature difference of 64 nodes at time interval n.) using all available measurements up to $y(n)$ (Measurement of of HTF temperature difference at receiver outlet, δx_{127} at time interval 1 to interval n .)

If we define coefficients in Equation (4.1) as in Equation (4.6)

$$\bar{A} = \begin{bmatrix} -(A+Bu_1^*) & A & 0 & 0 \\ A & -E & 0 & 0 \\ Bu_1^* & 0 & -(A+Bu_1^*) & A \\ 0 & 0 & A & -E \\ \vdots & \vdots & \vdots & \vdots \\ 0 & 0 & 0 & 0 \\ 0 & 0 & 0 & 0 \end{bmatrix} \begin{bmatrix} 0 & 0 & 0 & 0 \\ 0 & 0 & 0 & 0 \\ 0 & 0 & 0 & 0 \\ 0 & 0 & 0 & 0 \\ \vdots & \vdots & \vdots & \vdots \\ Bu_1^* & 0 & -(A+Bu_1^*) & A \\ 0 & 0 & A & -E \end{bmatrix} \tag{4.6}$$

$$\bar{B} = \begin{bmatrix} -Bx_1^* \\ 0 \\ Bx_1^* - Bx_3^* \\ 0 \\ \vdots \\ Bx_{127}^* - Bx_{128}^* \\ 0 \end{bmatrix} \tag{4.7}$$

$$\bar{C} = \begin{bmatrix} 0 & \cdots & 0 & 1 & 0 \end{bmatrix} \tag{4.8}$$

Based on above assumption, the objective is to minimize the system steady-state error covariance matrix as in Equation (4.9).

$$P = \lim_{t \to \infty} E\left((\delta x - \delta\hat{x})(\delta x - \delta\hat{x})^T\right) \tag{4.9}$$

The optimal solution of the system can be written as in Equation (4.11).

$$\delta\dot{\hat{x}} = \bar{A}\delta\hat{x} + \bar{B}\delta u_1 + L(\delta y - \bar{C}) \tag{4.10}$$

$$\delta\dot{\hat{y}} = \bar{C}\delta\hat{x} \tag{4.11}$$

With filter gain matrix L determined by Riccati Equation (4.12)

$$L = (P\bar{C}^T + GN_n)R_n^{-1} \tag{4.12}$$

4.4 Disturbance Rejection Model: LQG Design by Employing Kalman Filter+LQR

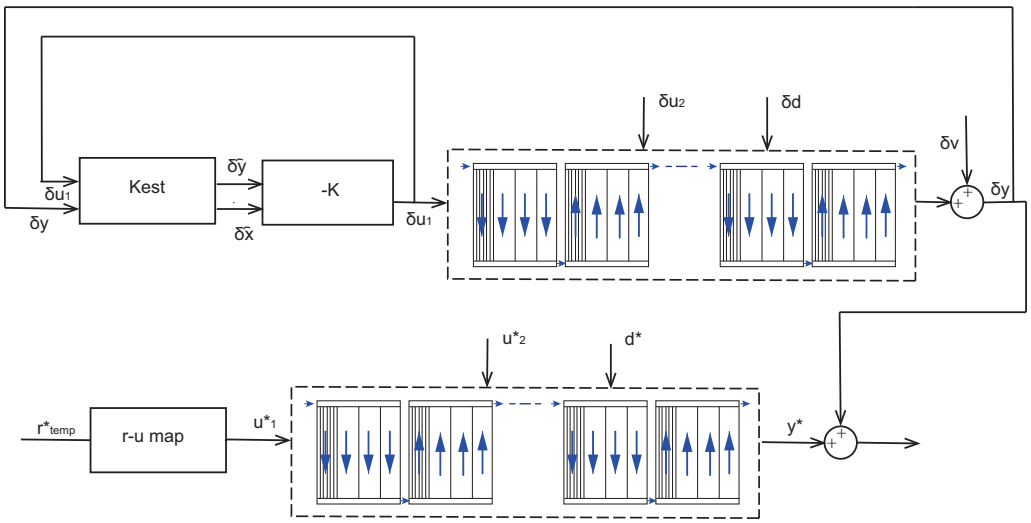

Figure 4.2. LQG regulator schematic for receiver dynamics with small disturbance

Figure 4.2 gives the schematic of LQG regulator design for receiver dynamics with small disturbances: Solar intensity fluctuation δu_2 around its nominal value u_2^* and ambient temperature fluctuation δd around its normal value d^*.

In the milliseconds to seconds level, the Kalman filter gain can be assumed as steady state gain and limit, and the separation principle for linear system holds for Equations (4.1) and (4.2). Therefore, the LQG regulator design for the system can be divided into two steps:

1. First, calculate estimate the full state $\delta\hat{x}$ using the available information, regulator control law δu_1 and system measured output δy.

2. Secondly, apply the LQR controller, using the estimation in place of the true (now unknown) state .

If we used the estimated states Equation (4.11) from Kalman filter to construct LQR controller as shown in figure 4.2, the LQR objective function from Equation (3.5) can be rewritten as (4.13).

$$J = \frac{1}{2}\delta\hat{x}^T(t_1)F(t_1)\delta\hat{x}(t_1) + \int_{t_0}^{t_1}(\delta\hat{x}^T Q\delta\hat{x} + \delta u^T R\delta u)dt \tag{4.13}$$

with control law $\delta u_1 = -K\delta\hat{x}$ and initial condition $\delta\hat{x}(t_0) = \delta x^*$

The regulator dynamics can be updated as:

$$\delta\dot{\hat{x}} = [\bar{A} - L\bar{C} - \bar{B}K] + L\delta y \tag{4.14}$$

It can be seen that both the control law and the dynamical update equations now are a function of estimated states rather than the actual states.

Figure 4.3 gives the plot of system perturbations as well as the HTF outlet temperature fluctuation with these system perturbations. The disturbances in subplot 1 includes solar intensity fluctuation δu_2, ambient temperature fluctuation δd and temperature measurement noise δv. The covariance of these system disturbance are 20, 5 and 4 respectively. Subplot 2 is the HTF outlet temperature with respect to those disturbances.

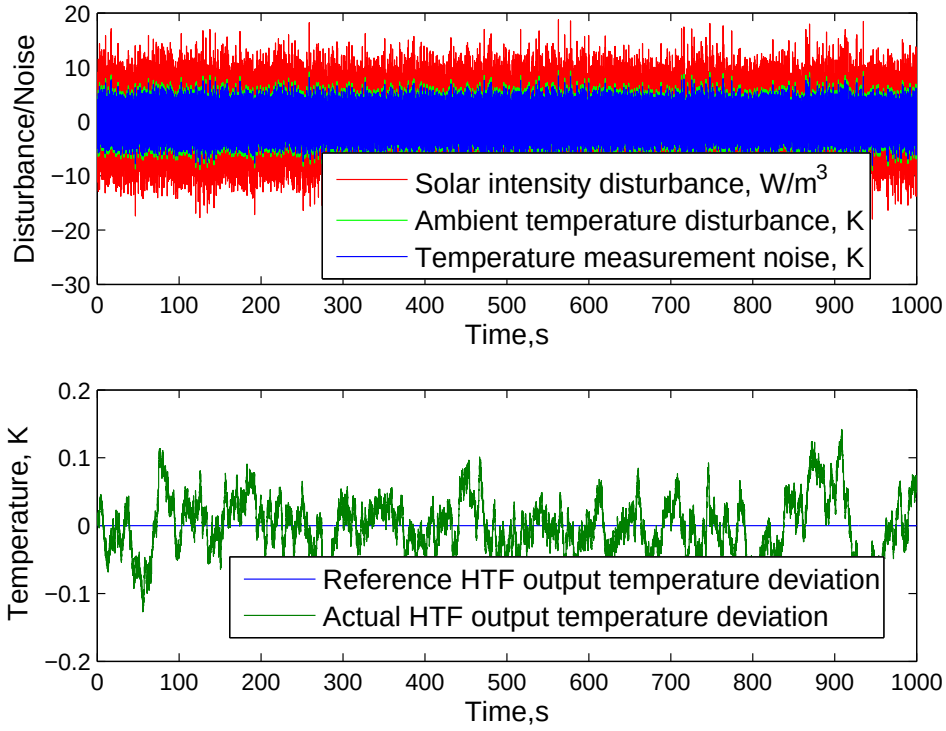

Figure 4.3. Disturbance/Measurement noise level and HTF outlet temperature with LQG regulator design

4.5 Reference Tracking Model: LQG Design by Employing Kalman Filter+LQI

In previous sections, we introduced LQR controller design for system without disturbance, we also introduced LQG controller employing Kalman filter and LQR design. LQR is balancing its output performance and disturbance rejection ability by setting the correct ratio between matrix Q and matrix R However, by natural the classical LQR is a static state feedback control law ($\delta u = -Kx$) without an integral term for the error signal. This may result in a poor controller performance when the system is tracking a non-zero step reference in the presence of system disturbance and measurement noise. We can improve on the tacking performance by introducing a term involving the historical integral information of output y. — Therefore, we

use LQI (as shown in figure 4.4 instead of LQR in this section to enhance controller reference tracking ability.

The integral error and its state space equations are as follows:

$$\delta\epsilon(t) = \int_0^t (\delta r(\tau) - \delta y(\tau))d\tau \tag{4.15}$$

$$\delta\dot{\epsilon}(t) = \delta r(t) - \bar{C}\delta x(t) \tag{4.16}$$

The system state space function including error dynamics can therefore be written as:

$$\begin{bmatrix} \delta\dot{x}(t) \\ \delta\dot{\epsilon}(t) \end{bmatrix} = \begin{bmatrix} \bar{A} & 0 \\ -\bar{C} & 0 \end{bmatrix} \begin{bmatrix} \delta x(t) \\ \delta\epsilon(t) \end{bmatrix} + \begin{bmatrix} \bar{B} \\ 0 \end{bmatrix} \delta u_1(t) + \begin{bmatrix} 0 \\ I \end{bmatrix} \delta r(t) \tag{4.17}$$

If we define $\delta z(t) = \begin{bmatrix} \delta x(t) \\ \delta\epsilon(t) \end{bmatrix}$, the new control law would be $u = -K\delta z$.

The system quadratic cost function of LQI controller would be:

$$J = \int_0^{\inf} (\delta z^T Q_i \delta z + \delta u^T R_i \delta u + 2\delta z^T N_i \delta z)dt \tag{4.18}$$

Where Q_i, R_i and N_i are the weighing matrix of LQI cost function.

The sketch of LQG servo controller is in figure 4.5, similarly, LQG servo controller also follows the principle of separations: We can still construct LQI controller first, and then update each states with the estimated states & system outputs constructed from Kalman filter. If we combine Equations (4.11) and (4.17), the control law of LQG servo controller is $\delta u_1 = -[K_x, K_i][\delta\hat{x}; \delta\epsilon]$, and the state space equations can be written as:

$$\begin{bmatrix} \delta\dot{\hat{x}}(t) \\ \delta\dot{\epsilon}(t) \end{bmatrix} = \begin{bmatrix} \bar{A} - \bar{B}K_x - L\bar{C} & -BK_i \\ 0 & 0 \end{bmatrix} \begin{bmatrix} \delta\hat{x}(t) \\ \delta\epsilon(t) \end{bmatrix} + \begin{bmatrix} 0 & L \\ I & -I \end{bmatrix} \begin{bmatrix} r \\ y \end{bmatrix} \tag{4.19}$$

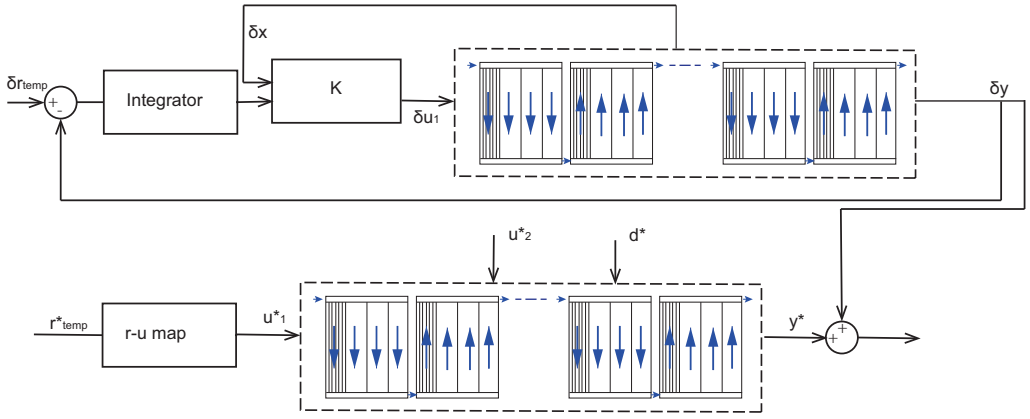

Figure 4.4. LQI controller schematic for receiver dynamics with small disturbance

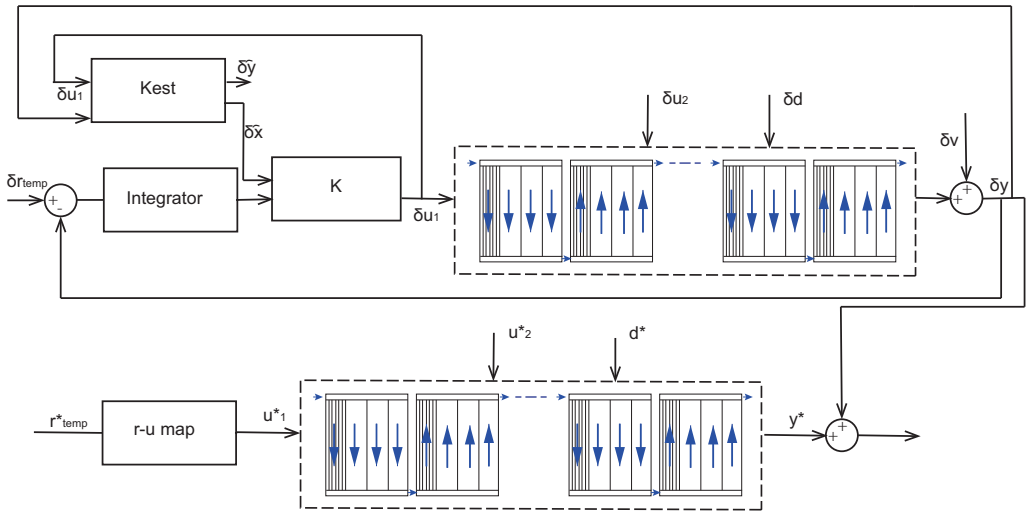

Figure 4.5. LQG reference controller schematic for receiver dynamics with small disturbance

Figure 4.5 gives a controller design for receiver dynamics with small disturbance. The disturbances in subplot 1 includes solar intensity fluctuation δu_2, ambient temperature fluctuation δd and temperature measurement noise δv. The covariance of these system disturbance are 20,5 and 4 respectively. Subplot 2 is the step increase

of 5K in reference HTF outlet temperature and system performance with respect to this reference input change, under disturbance.

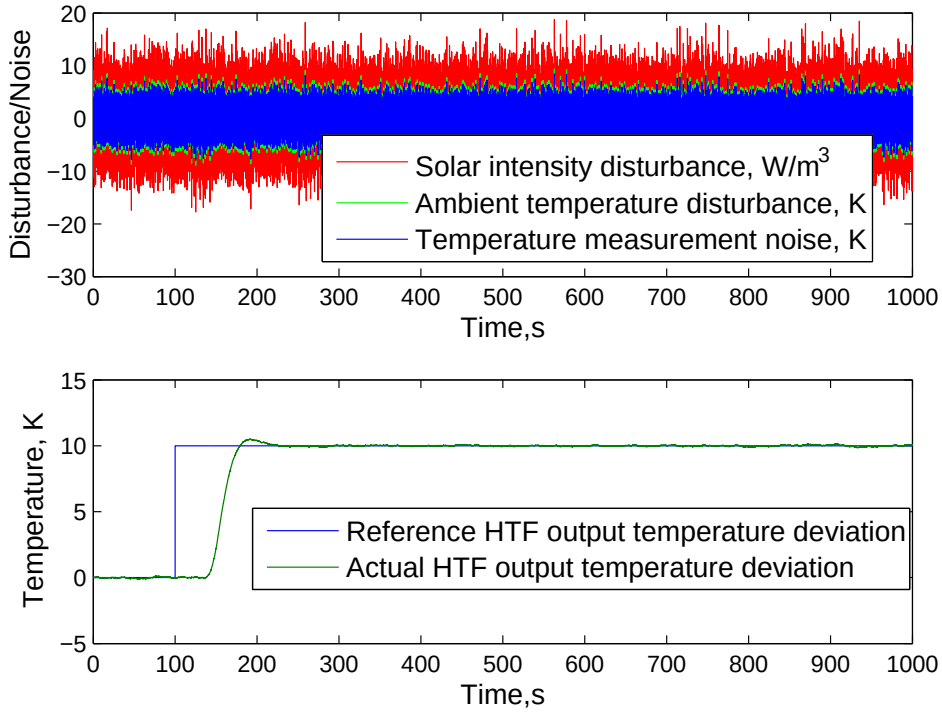

Figure 4.6. LQG regulator schematic for receiver dynamics with small disturbance

4.6 System Stability and Robustness Comparison Among Different Controllers

In general, the LQR is a more stable and robust controller compared to LQG, but the stability and robustness of LQG can be enhance by either constrain the authority of LQG control law or by integrating the dynamics of disturbance (if known) into the close loop system. Table 4.1 gives a summary of the stability and robustness comparison of three controllers. $Q > 0$ and $R > 0$ are assumed in the table, which is consistent with the Q and R matrix we use in those three controllers design.

It needs to be pointing out that:

Table 4.1. Controller stability and robustness comparison

-	*Stability*	*Robustness*
LQR	Asymptotically stable	Gain margin inf, phase margin 60^o [61]
LQG regulator	Conditionally stable	Not guaranteed, can be improved
LQG servo controller	Conditionally stable	Not guaranteed, can be improved

1. *The stability of the LQG is conditional.*

   LQG is considered as asymptotic stable only when the we have perfect knowledge of system parameters. This means the coefficients of state estimator from Equation (4.11) and the coefficients of LQR/LQI dynamics as in Equation (4.17) should be stable. i.e. $\bar{A}_{estimator} = \bar{A}_{controller}, \bar{B}_{estimator} = \bar{B}_{controller}$ ..., which is the case in our previous controllers design. In this case,

   (a) Estimator error affects state response.

   (b) Actual states do not affect error propagation.

   (c) System disturbance and measurement noise affect the estimator error and actual states equally.

   The system is therefore stable since all the sub-matrix of the state coefficients in Equation (4.17) are stable.

2. *The robustness of LQG is not guaranteed, but can be improved.*

   If the system parameters are uncertain, i.e. $\bar{A}_{estimator} \neq \bar{A}_{controller}, \bar{B}_{estimator} \neq \bar{B}_{controller}$ ..., the close loop system and estimator response are coupled and uncertainty parameters affect the close loop system eigenvalues. The detailed derivation of equations has been illustrated as in [62] and [63].

   LQR with loop transfer recovery (LQG/LTR) is commonly used solution to enhance the robustness of LQG [64] [65]. The general idea is to reduce the

system sensitivity function by increasing the system process noise [66]. The pre-requests for LQR/LTR [67] are

(a) Number of open loop system input (δu_1) is equal to system output (δy).

(b) Plant (receiver dynamics) has no unstable zero.

Our plant model meets both requirements, making LQG/LTR a good candidate for improving the system robustness.

Other methods includes the $H\infty$ controller design, which assumes the worst possible perturbation to the plant at all time in the process of controller design [68]; and design of disturbance based filter if the disturbance dynamics can be well defined.

But in all the methods mentioned above, the enhancement of system robustness is at the sacrifice of controller performance.

5. APPLICATIONS

5.1 Life Cycle Improvements

Our overall model permits direct estimation from measurements of material stress and strain levels in the CSP power tower due to various transients–either at startup and shutdown or due to clouds. The important portion of strain here is thermal strain which can be written as a function of the states in our model.

$$\epsilon_z = \alpha(T_z - T_0) \tag{5.1}$$

where ϵ_z is the thermal strain along z axis, α is the coefficient of thermal expansion, which is $11.0 \times 10^{-6} - 13.0 \times 10^{-6} m/mK$ depends on compositions. T_z and T_0 are temperatures at z position and 0 respectively.

Material life cycle models are based on the number of cycles at various levels of stress which is proportional to the strain obtained above via Hooke's law. The remaining life of any material decreases with each cycle depending upon the maximum stress level in the cycle and the mean stress in the cycle. According to previous work [69], the total strain (which is defined as $\epsilon/2$ versus fatigue life (which is denoted as N_f) for annealed AISI-SAE 4340 steel can be described by empirical Equation (5.2)

$$\frac{\epsilon_z}{2} = 0.58(2N_f)^{-0.57} + 0.0062(2N_f)^{-0.09} \tag{5.2}$$

With these equations, we can keep track of the instant panel fatigue life. Figure 5.1 gives the instant strain level plot of inlet and outlet headers with LQR designed as in figure 3.6—System with equilibrium point $u_1^* = 450kg/s$, $x_{127}^* = 847.15K$ and a step-input of $10K$. x axis of the figure is time in seconds, and y axis is instant life cycle. Start from figure 3.6, we first calculate the instant thermal strain between

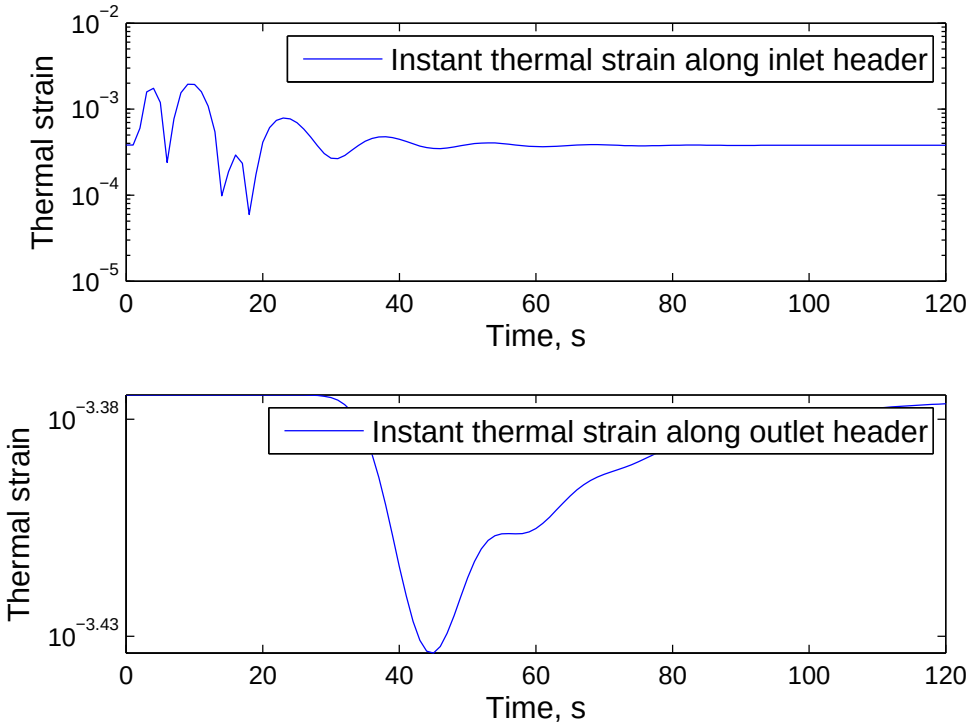

Figure 5.1. Instant thermal strain of inlet and outlet headers with LQR shown in Figure 3.6.

two adjunct nodes (or adjunct panels since the length of nodes and panels are the same.) using Equation (5.1). For instance, the instant thermal strain in subplot 1 of figure 3.6 would be the strain between node 1 and the tube before receiver, the instant thermal strain in subplot 2 of figure 3.6 would be the thermal strain between node 63 and node 64 (Outlet node). Using the maximum level of strain reached in a cycle, we can estimate the remaining life of the panel in real time. We can also design the control to maximize remaining life. Given that the dynamics of the CSP power tower and that of power production are separated by the molten salt tank, we need not constrain this optimization of the control.

We can see from figure 3.6 and figure 5.1 that the maximum instant temperature difference within all panels is $165.87K$ at $t = 9.46s$, this maximum instant temperature corresponds to a maximum instant thermal strain ϵ_{max} within the panel according

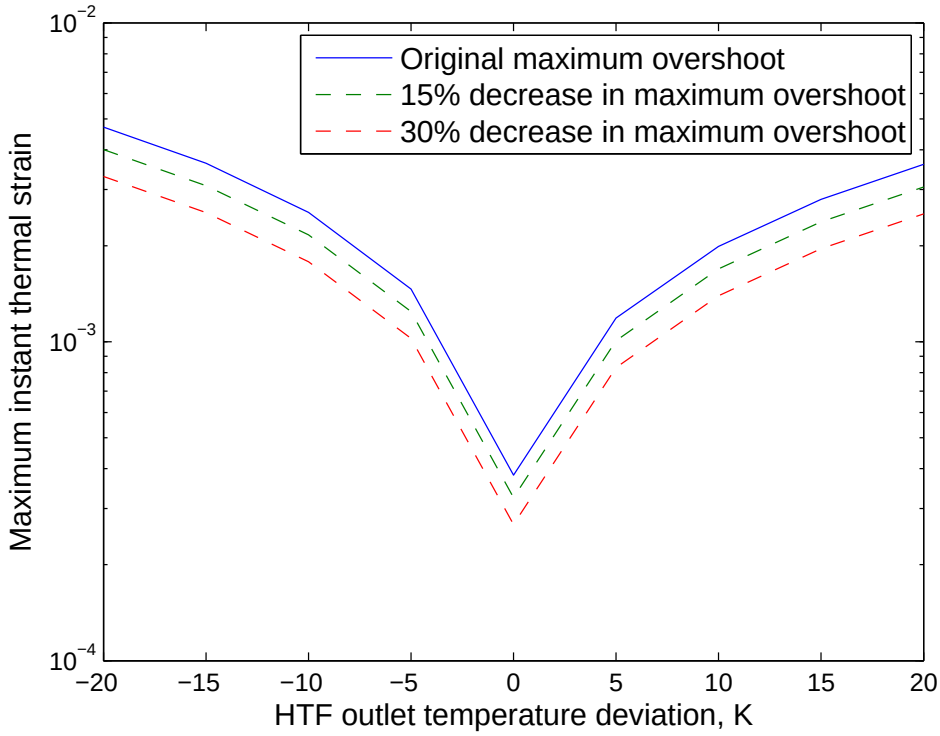

Figure 5.2. Relationship between HTF outlet temperature deviation r and maximum instant thermal strain ϵ^{max}.

to Equation (5.1) and therefore corresponds to a minimum instant fatigue life N_f^{min} according to Equation (5.2) at the same time. By changing the desired reference input to the receiver control model, we have build up relationship between steady state HTF outlet temperature deviation δT_{max} and minimum instant panel lift cycle N_f^{min} as is shown in figure 5.2. In this figure, x axis is the HTF outlet temperature deviation with respect to nominal value x_{127}^* in K, y axis is the minimum instant panel life cycle. Figure 5.2 indirectly gives the potential life cycle increase with controllers which can decrease the maximum temperature overshoot by 15% and 30% respectively.

5.2 Electricity Load and Price Forecasting Using Neural Network

We divide the electricity load forecasting procedure into two steps: the calibration part and the forecasting part:

- **Load calibration:** We make use of current weather condition (Dry bulb and dew point), seasonality (hour, weekday, holidays) and historical load (previous day, previous week) as calibration input, and use regression method as our calibration algorithm.
- **Load forecasting:** Once we get forecasting model from step one, we make use of forecast weather and load history data as model input to do load forecasting.

the price forecasting is similar, except that in both the calibration and forecasting parts, we use fuel energy price as model input as well (as is shown in figure 5.3).

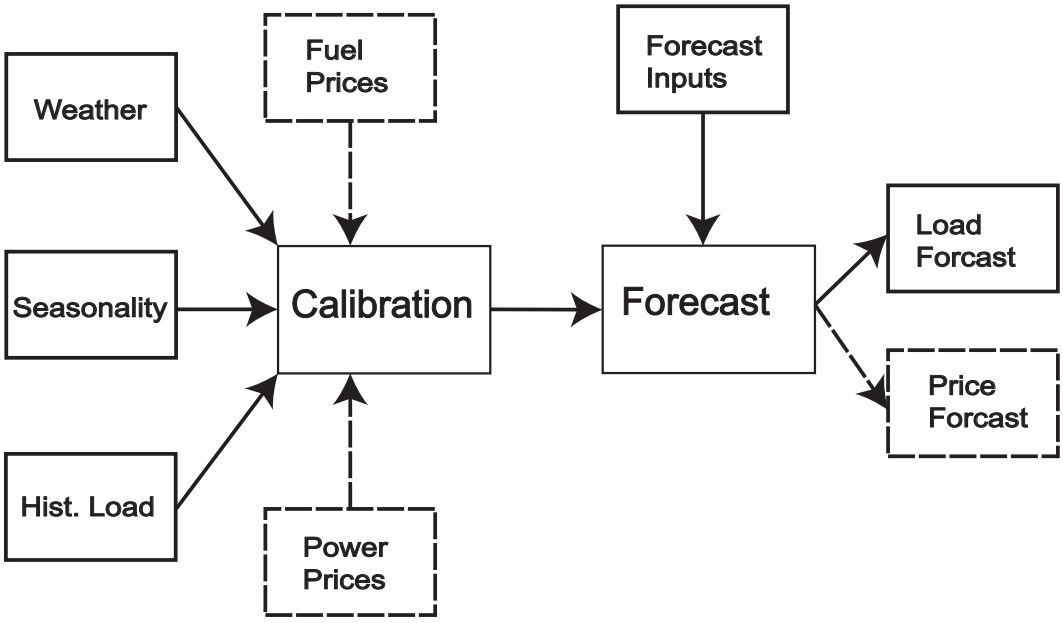

Figure 5.3. Load/Price calibration and forecast.

A neural network model of the data modeled by Equations (5.3) and (5.4) for short term electricity forecasting has been used for the simulation purpose [70]. Equation (5.3) gives the objective for minimizing the error between the desired and the

predicted outputs, and Equation (5.4) gives solutions for network weights. W in the equations represents vectors of all weights in the network (In our example, it represents weights for all inputs including weather conditions, seasonality and historical data, etc.). J in Equation (5.4) represents Jacobian vector of derivatives of the error to each weight, μ is a scalar making Equation (5.4) solvable.

$$E(W + \delta W) = E(W) + \frac{\partial E}{\partial W}\delta W + O(n), \tag{5.3}$$

$$\delta W = -[JJ^t + \mu[I]]^{-1}JE(W). \tag{5.4}$$

The quality of the model is evaluated using MAPE (Mean absolute percentage error), which is defined as

$$MAPE = \frac{100\%}{n}\sum_{t=1}^{n}|\frac{\hat{q}_t - q_t}{q_t}|. \tag{5.5}$$

In Equation (5.5), n represents number of load samples, $\hat{q}_t$ and q_t represents estimated load and real load respectively.

Figure 5.4 gives the load forecast results utilizing neutral network tree model described in figure 5.3. The load and price data we used for model training is from New England ISO [71] from 2005 to 2007 and the prediction model is validated by calculating the MAPE of the predicted data with actual demand data in the year of 2008.

5.3 Electricity Load and Price Forecasting Using Regression Tree

A bagging regression tree model can be used for simulating the short term electricity forecasting [72]. Bootstrap aggregation, or bagging [73], is often used to reduce the variance associated with prediction process, and thereby improve the prediction accuracy.

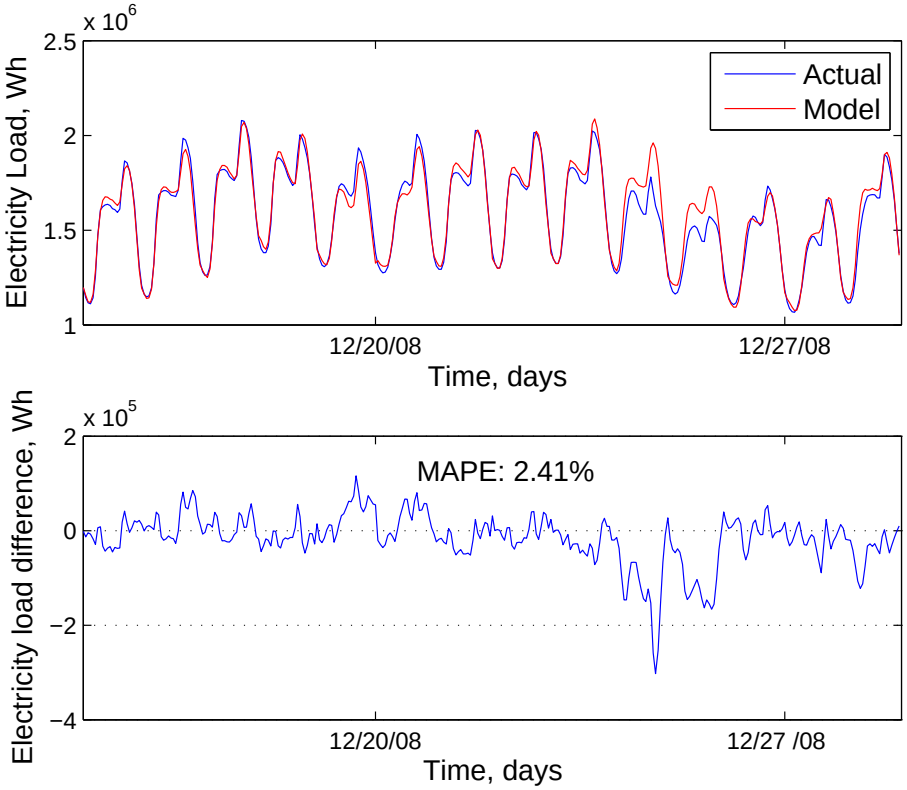

Figure 5.4. Load forecast and MAPE evaluation for neural network prediction model (12/15/2008-12/29/2008).

The idea is simple: The bootstrap samples are drawn from the available electricity load data, which has been pre-sorted according to weather, seasonality and historical data. Then apply a set of regression trees each with a different set of rules for performing the non-linear regression. Next we combine the results by averaging for regression and simple voting for classification. Following these steps we can finally obtain the overall prediction, with reduced variance due to the averaging. The importance of different predictors can be evaluated according to their out-of-bag estimates.

In the bagging process, roughly 37% of the original observations are left out as out-of-bag observation. The quality of the prediction model can be evaluated using out-of-bag error evaluation, which is defined as

$$\hat{\epsilon}_{ob} = \frac{\sum_{i=1}^{n} M_N^{-1} \sum_{k=1}^{N} f(\cdot)_{|X_i, Y_i \notin S^k} |Y_i - \hat{g}^{*k}(X_i)|^2}{n}. \tag{5.6}$$

where M_N is defined as

$$M_N = \sum_{i=1}^{N} f(\cdot)_{|X_i, Y_i \notin S^k} \tag{5.7}$$

In above equations, $\hat{\epsilon}_{ob}$ is the out-of-bag error for bagging regression tree, S_k is the union of all estimators whose original sample indices got resampled in the kth bootstrap sample. They other parameters in the above two equations are defined in Appendix.

1. *Create test matrix and target function for bagging*

   The influence factors in figure 5.3 and the electricity load history data would be sorted into pairs (X_i, Y_i, where $i = 1, 2, 3..., n$. X_i is the 7 dimensional matrix including: weather condition (Dry bulb and dew point), seasonality (hour, weekday, holidays) and historical load (previous day average ,same hour previous day, same hour same day previous week previous week). Y_i is the electricity load. The system target function would be: $E[Y|X = x]$.

2. *Construct regression model estimators*

   If we define the estimator equation to be

   $$\hat{g}(\cdot) = f\left(X_i, Y_i\right)) \tag{5.8}$$

   The simplest estimator with only one split and two nodes would be,

   $$\hat{g}(X = x) = \hat{\alpha_1} f(\cdot)_{|x<\hat{d}} + \hat{\alpha_2} f(\cdot)_{|x \geq \hat{d}} \tag{5.9}$$

   where we have $\hat{\alpha_1}$, $\hat{\alpha_2}$ and $\hat{d}$ defined as

   $$(\hat{\alpha_1}, \hat{\alpha_2}, \hat{d}) = argmin_{\alpha_1, \alpha_2, d} \sum_{i=1}^{i=n} (Y_i - \alpha_1 f(\cdot)_{|x<d} - \alpha_2 f(\cdot)_{|x \geq d}) \tag{5.10}$$

3. *Apply bagging algorithm to regression predictors*

   (a) *Construct a bootstrap sample* (X_1^*, Y_1^*),...,(X_n^*, Y_n^*)
   A bootstrap sample of the data (X_1, Y_1), . . . ,(X_n, Y_n) is constructed by repeating drawing n samples from data with replacement.

   (b) *Compute the regression estimator for bootstrap samples* $\hat{g}^*$ We can construct this estimator using the estimator equation as in Equation (5.8), the new equation would be:

$$\hat{g}^*(\cdot) = f\left(X_i^*, Y_i^*\right)) \tag{5.11}$$

   (c) *Compute the bagging estimator* $\hat{g}_{bag}(\cdot)$ The bagging estimator is a simple voting among all regression estimators generated by repeat step 1 and 2.

$$\hat{g}_{bag}^*(\cdot) = \frac{\sum_{k=1}^{N} \hat{g}^*(\cdot)_k}{N} \tag{5.12}$$

   where N is the number of execution times of step 1 and 2, $\hat{g}^*(\cdot)_k$ is the regression estimator from the kth repeats.

4. *Regression tree pruning.*
   The regression tree is always prune to reduce the complexity of the trees. The basic approach of pruning is to remove a subtree and evaluate the reduction of model errors at each split node.

Figure 5.5 gives the load forecast results utilizing regression tree model described in figure 5.3. The load and price data we used for model training is from New England ISO [71] from 2005 to 2007 and the prediction model is validated by calculating the MAPE of the predicted data with actual demand data in the year of 2008.

Figure 5.6 gives the regression tree structure, to make the tree structure more easier to interpret, we pruned the tree to a simple tree of 5 levels.

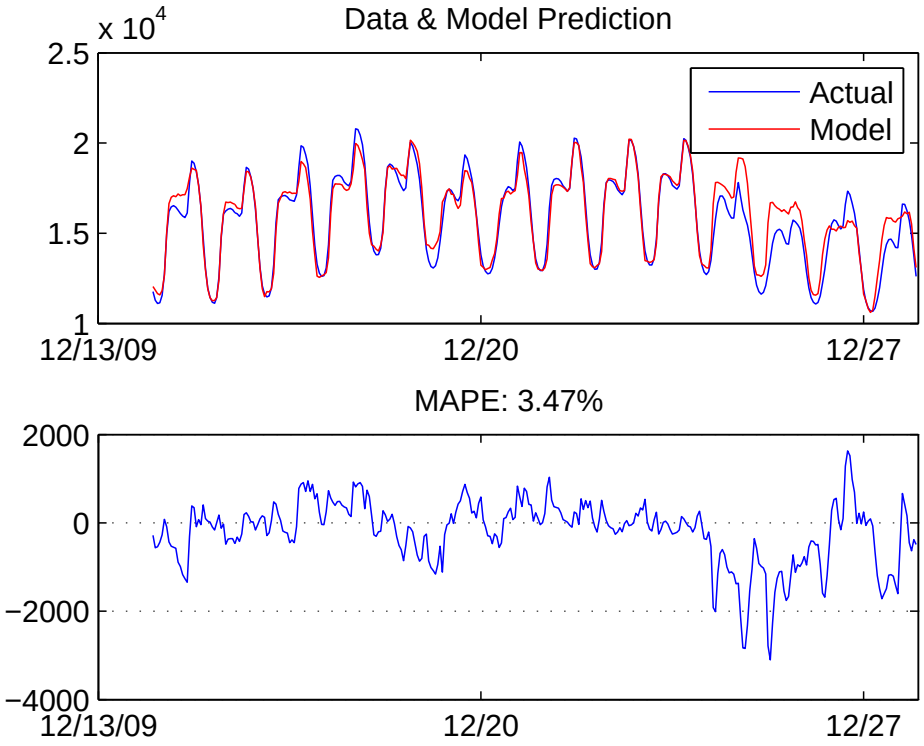

Figure 5.5. Load forecast and MAPE evaluation for bagged regression tree prediction model (12/15/2008-12/29/2008).

Figure 5.7 gives the weight of each predictors, it can be seen that the most important predictors are DryBulb and Weekdays (Weather the day of interest is weekdays or not).

Figure 5.8 gives the out-of-bag regression error as a function of number of grown trees in the ensemble, with minimum leaf size of each regress tree to be 10, 20, 40, 50.

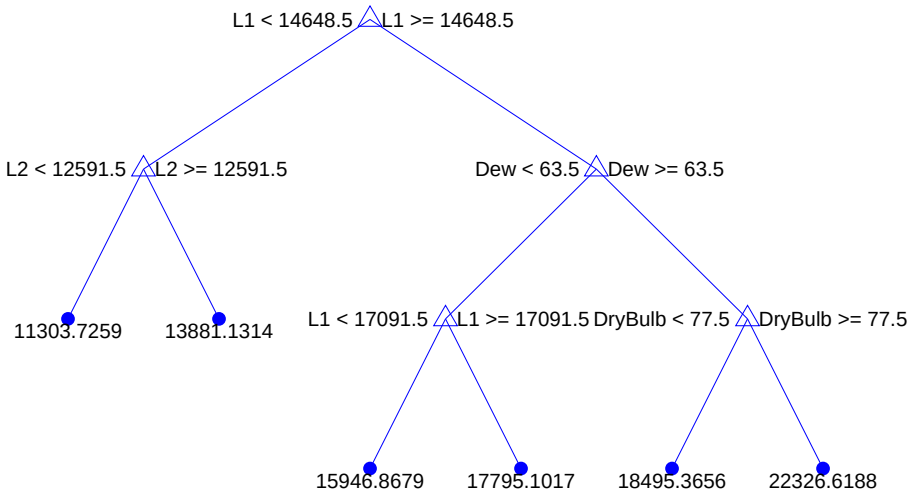

Figure 5.6. Load forecast regression tree structure, prune to level 5.

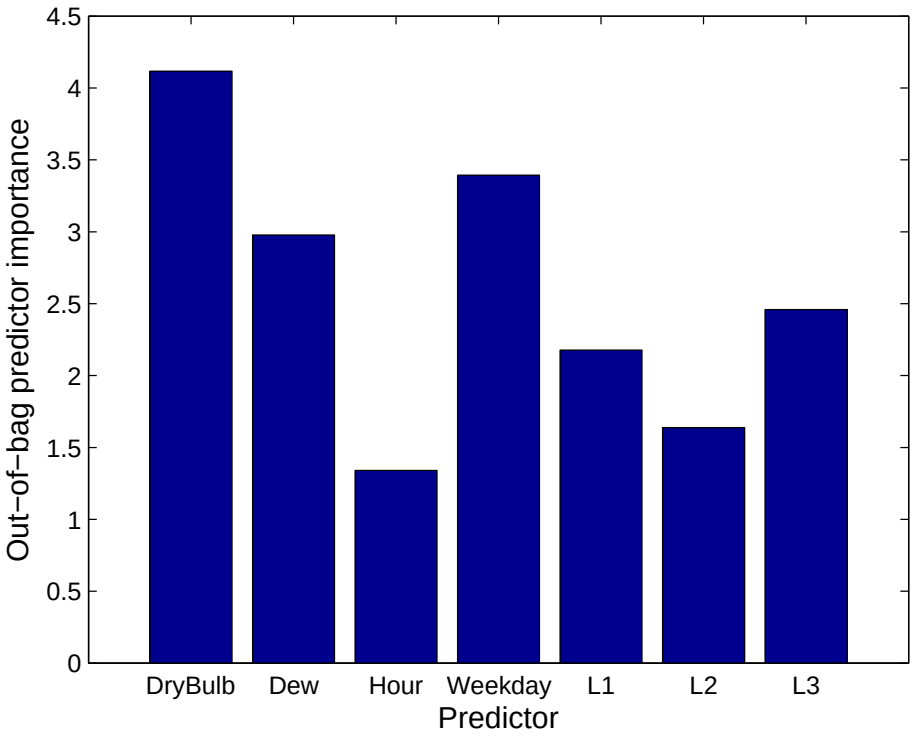

Figure 5.7. Predictor weight of load forecast bagged regression tree.

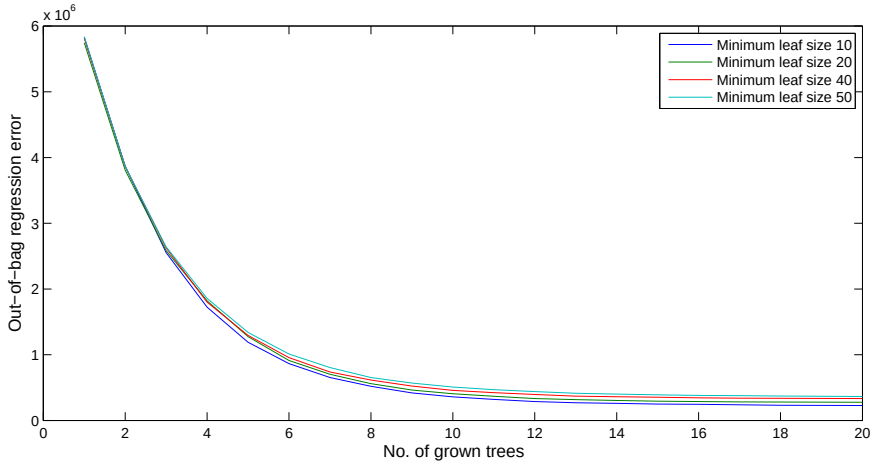

Figure 5.8. Load forecast bagged regression tree, Out-of-Bag regression error as function of No. of grown trees.

6. CONCLUSIONS

Conclusion We have developed a milliseconds resolution dynamical model for CSPs with detailed components including solar reflectors (heliostats), power towers, salt tanks, boiler, turbines, generators, piping as well as instant fatigue life model and demand forecast model. This integrated model platform allows researchers to run different control and optimization algorithms in real time and test their impact on system transients—which are the major cause of system failure and life cycle reduction. We have also shown in the paper that with proper control and optimization algorithm applied to the model, the panel life time can be increased and therefore the system LCOE may be reduced as well, making CSP plants more financially competitive with the traditional coal fired plants.

We have demonstrated a three-level controller architecture using multi-input-multi-output (MIMO) control for CSP plants that can be implemented on existing plants to improve performance, reliability, and extend the life of the plant. This architecture makes the optimization of the performance on multiple time scales including: reactive level (regulation to temperature set points), tactical level (adaptation of temperature set points), and strategic level (trading off fatigue life due to thermal cycling and current production) possible. This controller contribute significantly towards the Sunshot goal of 0.06/kWh(e), while responding to both market dynamics and changes in solar irradiance such as due to passing clouds. The controller also takes into consideration of plant disturbance and measurement noise in the controller design.

Future work This integrated CSP model provides a platform that allows more interesting problems to be quickly studied. Few of the interesting problems that can be easily implemented on this platform would be:

1. LQR/LTR and $H\infty$ controller design to enhance receiver controller stability and robustness.

2. Linear Parameter Varying (LPV) and Linear Matrix Inequalities (LMI) controller design for large scale disturbance and middle time scale optimization for heliostat-receiver subsystem.

3. Integration of PV and CSP for electricity output optimization.

4. Economics and environment trade-off for heliostat field optimization.

5. Heat storage design optimization based on electricity supply-demand optimization.

6. Modelling of CSP trough system and controllers design for this system.

LIST OF REFERENCES

LIST OF REFERENCES

[1] B. Canavan M. Mendelsohn, T. Lowder. Utility-scale concentrating solar power and photovoltaic projects: A technology and market overview. Technical report, National Renewable Energy Laboratory (NREL), Golden, CO., 2012.

[2] K. Johnson and S. Page. Utility-scale solar projects in the united states operating, under construction, or under development. Technical report, Solar Energy Industries Association (SEIA), 2011.

[3] T. Kimbis and S. Fenn. Solar market insight report 2012, q1. Technical report, Solar Energy Industries Association (SEIA), 2012.

[4] B. Hoffschmidt, S. Alexopoulos, C. Rau, J. Sattler, A. Anthrakidis, C. Boura, B. Connor, and P. Hilger. Concentrating solar power. In *Comprehensive Renewable Energy*, pages 595 – 636. Elsevier, Oxford, 2012.

[5] J. V. Scoter and D. Rogers. Sierra suntower fact sheet. Technical report, eSolar Co., 2010.

[6] M. Mehos. Genesis solar energy project fact sheet. Technical report, National Renewable Energy Laboratory, 2009.

[7] T. Wendelin. Concentrating solar power projects: Solana. Technical report, National Renewable Energy Laboratory, 2010.

[8] P. K. Falcone. A handbook for solar central receiver design. Technical report, Sandia National Labs., Livermore, CA (USA), 1986.

[9] E. Sani, L. Mercatelli, P. Sansoni, L. Silvestroni, and D. Sciti. Spectrally selective ultra-high temperature ceramic absorbers for high-temperature solar plants. *Journal of Renewable and Sustainable Energy*, 4(3), 2012.

[10] G. Augsburger and D. Favrat. Modelling of the receiver transient flux distribution due to cloud passages on a solar tower thermal power plant. *Solar Energy*, 87:42 – 52, 2013.

[11] D. O. Harris, C. H. Wells, H. J. Grunloh, R. H. Ryder, J. M. Bloom, C. C. Schultz, and R. Viswanathan. Bless-boiler life evaluation and simulation system: A computer code for reliability analysis of headers and piping. *American Society of Mechanical Engineers, Pressure Vessels and Piping Division*, 251:17–17, 1993.

[12] G. Grossman and M. T. Heath. Simultaneous heat and mass transfer in absorption of gases in turbulent liquid films. *International Journal of Heat and Mass Transfer*, 27(12):2365 – 2376, 1984.

[13] G. J. Kolb, R. Davenport, D. Gorman, R. Lumia, R. Thomas, and M. Donnelly. Heliostat cost reduction. pages 1077–1084, 2007.

[14] S. A. Kalogirou. Solar energy collectors. In *Solar Energy Engineering*, pages 121 – 217. Academic Press, Boston, 2009.

[15] I. Reda and A. Andreas. Solar position algorithm for solar radiation applications (revised). Technical report, National Renewable Energy Laboratory, 2008.

[16] M. Schmitz, P. Schwarzbzl, R. Buck, and R. P.-Paal. Assessment of the potential improvement due to multiple apertures in central receiver systems with secondary concentrators. *Solar Energy*, 80(1):111 – 120, 2006.

[17] X. Wei, Z. Lu, W. Yu, and Z. Wang. A new code for the design and analysis of the heliostat field layout for power tower system. *Solar Energy*, 84(4):685 – 690, 2010.

[18] C. J. Noone, M. Torrilhon, and A. Mitsos. Heliostat field optimization: A new computationally efficient model and biomimetic layout. *Solar Energy*, 86(2):792 – 803, 2012.

[19] R. Pitz-Paal, N. B. Botero, and A. Steinfeld. Heliostat field layout optimization for high-temperature solar thermochemical processing. *Solar Energy*, 85(2):334 – 343, 2011.

[20] M. Berenguel, F.R. Rubio, A. Valverde, P.J. Lara, M.R. Arahal, E.F. Camacho, and M. Lapez. An artificial vision-based control system for automatic heliostat positioning offset correction in a central receiver solar power plant. *Solar Energy*, 76(5):563 – 575, 2004.

[21] M. Guo, Z. Wang, J. Zhang, F. Sun, and X. Zhang. Determination of the angular parameters in the general altitudeazimuth tracking angle formulas for a heliostat with a mirror-pivot offset based on experimental tracking data. *Solar Energy*, 86(3):941 – 950, 2012.

[22] J. J. Guo, J. Y. Wu, R. Z. Wang, and S. Li. Experimental research and operation optimization of an air-source heat pump water heater. *Applied Energy*, 88:4128–4138, April 2011.

[23] A. M. Clausing. An analysis of convective losses from cavity solar central receivers. *Solar Energy*, 27(4):295 – 300, 1981.

[24] N. Singh, S.C. Kaushik, and R.D. Misra. Exergetic analysis of a solar thermal power system. *Renewable Energy*, 19(12):135 – 143, 2000.

[25] A. Kurtbas and A. Durmust. Efficiency and exergy analysis of a new solar air heater. *Renewable Energy*, 29(9):1489 – 1501, 2004.

[26] M. J. Montes, A. Rovira, J. M. Martnez-Val, and A. Ramos. Proposal of a fluid flow layout to improve the heat transfer in the active absorber surface of solar central cavity receivers. *Applied Thermal Engineering*, 35(0):220 – 232, 2012.

[27] X. Yang, X. Yang, J. Ding, Y. Shao, F. G.F. Qin, and R. Jiang. Criteria for performance improvement of a molten salt thermocline storage system. *Applied Thermal Engineering*, 48(0):24 – 31, 2012.

[28] A. Gil, M. Medrano, I. Martorell, A. Lzaro, P. Dolado, B. Zalba, and L. F. Cabeza. State of the art on high temperature thermal energy storage for power generation. part 1 concepts, materials and modellization. *Renewable and Sustainable Energy Reviews*, 14(1):31 – 55, 2010.

[29] Z. Yang and S. V. Garimella. Thermal analysis of solar thermal energy storage in a molten-salt thermocline. *Solar Energy*, 84(6):974 – 985, 2010.

[30] S. Flueckiger, Z. Yang, and S. V. Garimella. An integrated thermal and mechanical investigation of molten-salt thermocline energy storage. *Applied Energy*, 88(6):2098 – 2105, 2011.

[31] A. Mawire, M. McPherson, R. R. J. van den Heetkamp, and S.J.P. Mlatho. Simulated performance of storage materials for pebble bed thermal energy storage (tes) systems. *Applied Energy*, 86(78):1246 – 1252, 2009.

[32] T. M. Sanderson and G. T. Cunningham. Performance and efficient design of packed bed thermal storage systems. part 1. *Applied Energy*, 50(2):119 – 132, 1995.

[33] L. F. Cabeza. Thermal energy storage. In *Comprehensive Renewable Energy*, pages 211 – 253. Elsevier, Oxford, 2012.

[34] M. Hannchen, S. Brckner, and A. Steinfeld. High-temperature thermal storage using a packed bed of rocks - heat transfer analysis and experimental validation. *Applied Thermal Engineering*, 31(10):1798 – 1806, 2011.

[35] D. A. Plautz and H. F. Johnstone. Heat and mass transfer in packed beds. *American Institute of Chemical Engineers*, 1(2):193–199, 1955.

[36] S. Holland. Hitec heat transfer salt. Technical report, Brenntag Company.

[37] E. E. Gonzo. Estimating correlations for the effective thermal conductivity of granular materials. *Chemical Engineering Journal*, 90(3):299 – 302, 2002.

[38] R. Ekbom. Application of hip/pm technique for gas and steam turbines. *Metal Powder Report*, 45(4):284 – 289, 1990.

[39] A. Chaibakhsh and A. Ghaffari. Steam turbine model. *Simulation Modelling Practice and Theory*, 16(9):1145 – 1162, 2008.

[40] J. M. Medina-Flores and M. Picon-Nunez. Modelling the power production of single and turbines. *Chemical Engineering Science*, 65(9):2811 – 2820, 2010.

[41] K. J. Astrom and R.D. Bell. Drum-boiler dynamics. *Automatica*, 36(3):363 – 378, 2000.

[42] W. M. Lin, C. C. Tsai, and C. H. Lin. Analysing the linear equivalent circuits of electromechanical systems for steam turbine generator units. *Generation, Transmission Distribution, IET*, 5(7):685 –693, july 2011.

[43] E. F. Fuchs and M. A.S. Masoum. Modeling and analysis of synchronous machines. In *Power Quality in Power Systems and Electrical Machines*, pages 155 – 207. Academic Press, Burlington, 2008.

[44] C. T. Abdallah. Electric grid control: Algorithms & open problems. Technical report, University of New Mexico, 2009.

[45] G. J. Nakoneczny and C.C. Schultz. Life assessment of high temperature headers. *Babcock & Wilcox, BR-1586*, 1995.

[46] G. Glatzmaier. Summary report for concentrating solar power thermal storage workshop: New concepts and materials for thermal energy storage and heat-transfer fluids, may 20, 2011. Technical report, National Renewable Energy Laboratory (NREL), Golden, CO., 2011.

[47] G. Kreisselmeier. Adaptive observers with exponential rate of convergence. *Automatic Control, IEEE Transactions on*, 22(1):2–8, 1977.

[48] M. Krstic, I. Kanellakopoulos, P. V. Kokotovic, et al. *Nonlinear and adaptive control design*, volume 8. John Wiley & Sons New York, 1995.

[49] P. A. Ioannou and J. Sun. *Robust adaptive control*. Courier Corporation, 1996.

[50] R. Marino and P. Tomei. *Nonlinear control design: geometric, adaptive and robust*. Prentice Hall International (UK) Ltd., 1996.

[51] K. B. Ariyur and M. Krstic. *Real-time optimization by extremum-seeking control*. Wiley-Interscience, 2003.

[52] J. Freeman T. Neises M. Wagner T. Ferguson P. Gilman N. Blair, A. P. Dobos and S. Janzou. *System Advisor Model (SAM)*. National Renewable Energy Laboratory, 2014.

[53] A. E. Gheribi, J. A. Torres, and P. Chartrand. Recommended values for the thermal conductivity of molten salts between the melting and boiling points. *Solar Energy Materials and Solar Cells*, 126:11 – 25, 2014.

[54] S. P Boyd, L. El Ghaoui, E. Feron, and V. Balakrishnan. *Linear matrix inequalities in system and control theory*, volume 15. SIAM, 1994.

[55] D. P Bertsekas. *Dynamic programming and optimal control*, volume 1. Athena Scientific Belmont, MA, 1995.

[56] E. J. Farmer and B. G. Liptak. Steam turbine controls. In *Process Control (Third Edition)*, pages 1442 – 1452. Butterworth-Heinemann, third edition edition, 1995.

[57] P. C Krause, O. Wasynczuk, S. Sudhoff, and S. Pekarek. *Analysis of electric machinery and drive systems*, volume 75. John Wiley & Sons, 2013.

[58] W.E. Bill Forsthoffer. Steam turbine control/protection systems. In *Forsthoffer's Rotating Equipment Handbooks*, pages 337 – 354. Elsevier Science, Oxford, 2005.

[59] W. Li, L. Vanfretti, and Y. Chompoobutrgool. Development and implementation of hydro turbine and governor models in a free and open source software package. *Simulation Modelling Practice and Theory*, 24:84 – 102, 2012.

[60] A. Khodabakhshian and R. Hooshmand. A new pid controller design for automatic generation control of hydro power systems. *International Journal of Electrical Power and Energy Systems*, 32(5):375 – 382, 2010.

[61] D. S. Naidu. *Optimal control systems*, volume 2. CRC press, 2002.

[62] K. J. Åström and B. Wittenmark. *theory and design*. Courier Dover Publications, 2011.

[63] J. S. Luo and A. Johnson. Stability robustness of the continuous-time lqg system under plant perturbation and noise uncertainty. *Automatica*, 29(2):485 – 489, 1993.

[64] H. Kwakernaak. Optimal low-sensitivity linear feedback systems. *Automatica*, 5(3):279–285, 1969.

[65] G. Stein and M. Athans. The lqg/ltr procedure for multivariable feedback control design. *Automatic Control, IEEE Transactions on*, 32(2):105–114, Feb 1987.

[66] J. C. Doyle and G. Stein. Multivariable feedback design: concepts for a classical/modern synthesis. In *IEEE Trans. on Auto. Control*. Citeseer, 1981.

[67] M. Athans. A tutorial on the lqg/ltr method. In *American Control Conference, 1986*, pages 1289–1296. IEEE, 1986.

[68] D. Simon. *Optimal state estimation: Kalman, H infinity, and nonlinear approaches*. John Wiley & Sons, 2006.

[69] B. Boardman. Fatigue resistance of steels. *ASM International, Metals Handbook. Tenth Edition*, 1:673–688, 1990.

[70] N. Kandil, R. Wamkeue, M. Saad, and S. Georges. An efficient approach for short term load forecasting using artificial neural networks. *International Journal of Electrical Power and Energy Systems*, 28(8):525 – 530, 2006.

[71] Historical electricity demand &price data. Technical report.

[72] R. Weron. *Modeling and forecasting electricity loads and prices: A statistical approach*, volume 403. John Wiley & Sons, 2007.

[73] L. Breiman. Bagging predictors. *Machine learning*, 24(2):123–140, 1996.

[74] C. Maffezzoni and F. Parigi. Dynamic analysis and control of a solar power planti dynamic analysis and operation criteria. *Solar Energy*, 28(2):105 – 116, 1982.

[75] T. Stoffel, D. Renné, D. Myers, S. Wilcox, M. Sengupta, R. George, and C. Turchi. Concentrating solar power: Best practices handbook for the collection and use of solar resource data (csp). Technical report, National Renewable Energy Laboratory (NREL), Golden, CO., 2010.

[76] N. Blair, M. Mehos, C. Christensen, and C. Cameron. Modeling photovoltaic and concentrating solar power trough performance, cost, and financing with the solar advisor model. *Solar 2008, American Solar Energy Society*, 2008.

[77] M.F. Rahman, D. Patterson, A. Cheok, and R. Betz. 34 - motor drives. In *Power Electronics Handbook (Third Edition)*, pages 915 – 991. Butterworth-Heinemann, Boston, third edition edition, 2011.

[78] S. Pumps. Physical principles. In *Centrifugal Pump Handbook (Third Edition)*, pages 1 – 26. Butterworth-Heinemann, Oxford, third edition edition, 2010.

APPENDIX

A. APPENDIX

A.1 Solar Radiation, Temperature, Electricity Load Sensing and Measurement

The Solar radiation and electricity loading profile serves as disturbance to the control architect, therefore in order to enhance the control quality of CSP plant, we need to first have a good measurement of current solar radiation and accurate electricity loading information.

A.1.1 Solar Radiation Measurement

As discussed in chapter 2, a cloud can reduce the solar radiation from sun significantly, as shown in figure A.1 from National Renewable Energy Laboratory, therefore the cloud passing by the concentrating solar plant can introduce irradiation transients, sustaining a strong thermal stress on receivers. This thermal stress can cause a decrease in receiver cyclic life and a decrease in solar absorption efficiency,as discussed in [74].

Therefore, it is essential to estimate and do a real-time measurement of solar irradiation, and develop control algorithm to avoid strong thermal stress.

Commonly used solar radiation measurement instrument includes:

Pyrheliometer : For direct normal solar radiation measurement.

Pyranometer : For global horizontal radiation measurement.

- **Thermopile detectors** :Slow, expensive, flat spectral response.
- **Thermopile detectors** :Fast, Low-Cost, with Reduced Spectral Response (figure A.2).

Shaded Pyranometer : For diffuse radiation measurement.

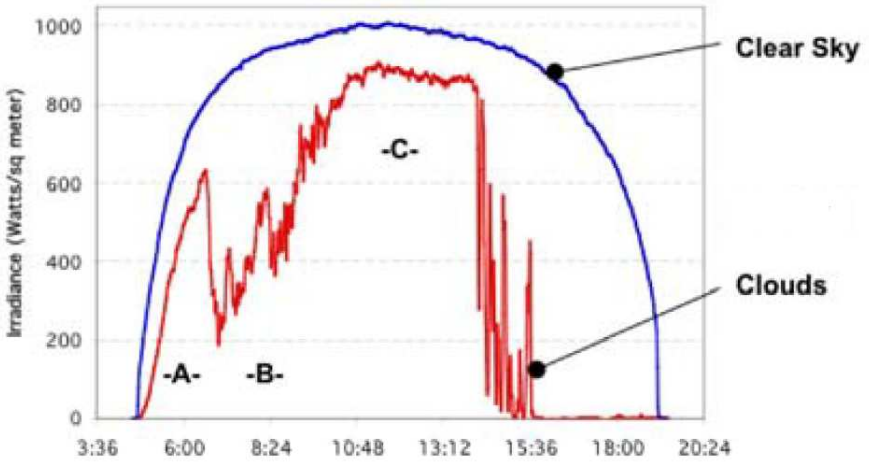

Figure A.1. Solar radiation for days with and without cloud.

Table A.1 gives a comparison of the two solar sensors. The research objective in solar radiation measurement is to choose adequate sensors for solar radiation measurement based on sensitivity, reaction time, linearity, bias, etc.

Table A.1. Advantage and disadvantage of thermopile detectors compared with photoelectric detectors [75].

	Photodiode	Thermopile
Electromagnetic Spectrum [nm]	400-1100	335-2200
Response Time	50 ms	$<$ 15s
Operating Temp. ^oC	-40 to 65	-40 to 80

A.1.2 Temperature Measurement

The measurement of ambient temperature, temperature distribution on CSP receiver, inlet and outlet temperature from thermal storage, feedwater steam temperature and boilder output temperature is essential in monitoring and control of CSP-steam turbine plant.

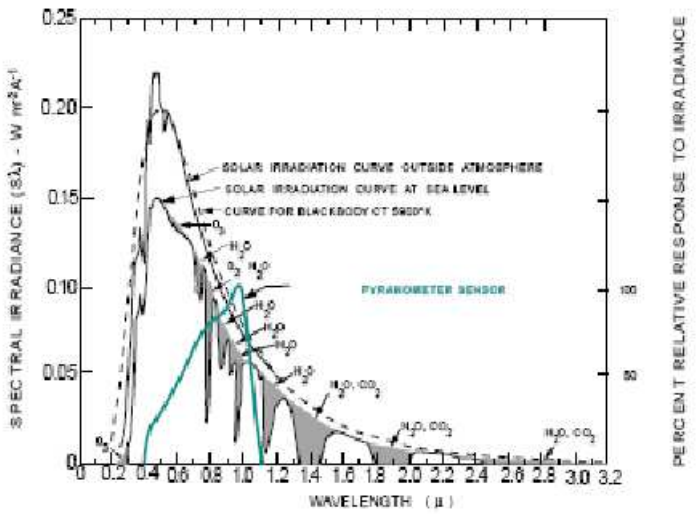

Figure A.2. Frequency response of photoelectric detectors.

Ambient temperature sensing and measurement :

The ambient temperature can be easily measured with Thermal Couple, RTD, or other sensor and instruments. Table A.2 gives a comparison of different ambient temperature sensors.

Table A.2. Ambient Temperature Measurement Comparison.

Criteria	Thermocouple	RTD	Thermistor
Temp Range (^oC)	-267 to 2316	-240 to 649	-100 to 500
Accuracy	Good	Best	Good
Linearity	Better	Best	Good
Sensitivity	Good	Better	Best
Response Time	Fast	Slow	Fast
Cost	Best	Good	Better

CSP receiver temperature sensing and measurement :

Commonly used technology in CSP receiver temperature sensing and measurement sensors are video cameras, of which , Beam Characterization System used by National Renewable Energy Laboratory [76] to plot thermal distribution of

CSP receivers for trough system, can also be extended to CSP tower system as well.

Beam Characterization System :

The system consists of the camera, frame grabber, and software. The beam characterization system measures the solar flux incident at receiver, and the figure A.3 gives the plot of concentrated sunshine on a target using Beam Characterization System.

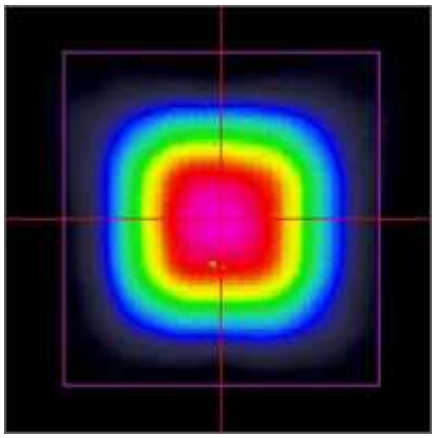

Figure A.3. Plot of concentrated sunshine on a target using Beam Characterization System.

HTF temperature sensing and measurement :

A.2 Motors Comparison

Motors employed in concentrating solar plants: For heliostat position control and for pmup driving, different specifications are required in these two subsystems.

Motors for heliostat position control :

In the heliostat position control system, the position of heliostats needs to be adjusted for higher level control optimization purpose, typical motor systems in usage for position control are stepper motors and servo motors, with characteristics comparison in table A.3

Table A.3. Servo motor vs Stepper motor [77].

Characteristics	Servo Motor	Stepper motor
Power Range	High	Medium
Efficiency	80%-90%	70%
Low Speed High Torque	Good	Good
High speed High Torque	Good	Bad
Power to Weight/Size ratio	Better	Good
Torque to Inertia Ratio	Better	Good
Overload Safety	Bad	Good
Repeatability	Good	Better

Motors for pumps :

Motors for pumps driving usually use AC source, since it has large rating available (can be up to 1 MW or higher). typical AC motors in usage are AC induction motors and AC synchronize motors, with characteristics comparison in table A.4.

Table A.4. AC induction motors vs AC synchronize motors [77].

Characteristics	AC induction motors	AC synchronize motors
Power Range	High	Medium
Efficiency	High	Higher
Speed Accuracy	Medium	High
Load torque variation	Slight variance	None
Power factor	0.5-0.9 lagging	Flexible
Start Current	High	Low
Start torque	Low	High
Cost	Low	High

A.3 Pumps Comparison

Pumps in concentrating solar plants models are used for working fluid flow rate control (molten salt and steam), so centrifugal pumps will be used for analysis. gener-

ally, there are three types of centrifugal pumps :Radial-flow pumps, Axial-flow pumps and Mixed-flow pumps, with characteristic comparison in table A.5.

Table A.5. Radial-flow pumps, Axial-flow pumps and Mixed-flow pumps comparison [78].

Characteristics	Radial flow pumps	Axial flow pumps	Mixed flow pumps
Enter direction	Along axial plane	Parallel to the rotating shaft	-
Exit direction	Right angles to the shaft(radially)	Parallel to the rotating shaft	-
Operation pressure	High	Low	Medium
Operation flow rate	Low	High	Medium

VITA

VITA

Luo,Qi received the Bachelor's degree from Shanghai Jiao Tong University (SJTU), Shanghai, China, in 2009. During 2008-2009, he was undergraduate exchange student in Purdue University. He is now a graduate student in Department of Mechanical Engineering, Purdue University, Indiana, USA. His current research interests include analysis and control of power system.